Synergistic reinforcement learning by cooperation of the cerebellum and basal ganglia

Abbreviated title: Synergy between cerebellum and basal ganglia

Tatsumi Yoshida[1]*, Hikaru Sugino[1]*, Hinako Yamamoto[1]*, Sho Tanno[1], Mikihide Tamura[1], Jun Igarashi[2], Yoshikazu Isomura[1†], Riichiro Hira[1†]

Affiliates:
1. Department of Physiology and Cell Biology, Graduate School of Medical and Dental Sciences, Institute of Science Tokyo, Tokyo, Japan
2. High Performance Artificial Intelligent System Research Team, Center for Computational Science, RIKEN, Saitama, Japan
* These authors equally contributed to this work.
† Corresponding authors.

Correspondence:
Riichiro Hira, M.D. Ph.D. rhira.phy2@tmd.ac.jp
Department of Physiology and Cell Biology, Graduate School of Medical and Dental Sciences, Institute of Science Tokyo, 1-5-45 Yushima, Bunkyo-ku, Tokyo, 113-8510, Japan.

Yoshikazu Isomura, Ph.D. isomura.phy2@tmd.ac.jp
Department of Physiology and Cell Biology, Graduate School of Medical and Dental Sciences, Institute of Science Tokyo, 1-5-45 Yushima, Bunkyo-ku, Tokyo, 113-8510, Japan.

Number of pages: 43

Number of figures, tables, multimedia, and 3D models (separately): 12, 3, 0, 0.

Number of words for abstract, introduction, and discussion (separately): 252, 826, 1781.

Conflict of interest statement: The authors have no conflicts of interest to declare.

Acknowledgements:
We thank T. Shimada, R. Mizuno, Reiko Hira for animal husbandry and genotyping, M. Kawabata, A. Rios, T. K. Fujita, Sakairi, S.L. Smith, J.N. Stirman, S. Aoki, A. Funamizu K. Ishizu, S. Tsutsumi, M. Morishima, T. Ishikawa, T. Yamazaki, H. Mori for technical advices and discussion. We also thank the editor and reviewers for helpful comments. This work was supported by JP22wm0525007 (RH), JP24wm0625405 (RH), JP19dm0207089 (YI) from AMED, JP24H02156

(RH), JP22H02731 (RH), JP20K22678 (RH), JP21B304 (RH), JP21H05134 (RH), JP21H05135 (RH), JP16H06276 (YI), JP21H0524 2(YI), JP19H03342 (YI), JP23H02589 (YI), and JP20H05053 (YI) from MEXT/JSPS, JPMJCR1751 (YI) from JST, Nakatani Foundation (RH), Shimadzu Foundation (RH), Takeda Science Foundation (RH), Takeda Science Foundation (YI), The Precise Measurement Technology Promotion Foundation (RH), Tateishi Science and Technology Foundation (RH), and Research Foundation for OptoScience and Technology (RH).

Author contributions:

R.H. conceived the project. T.Y. H.S. M.T. conducted electrophysiological experiments. S.T. conducted anatomical experiments. R.H. H.S. T.Y. M.T. analyzed electrophysiological data. H.Y. J.I., R.H. performed spiking neuron network simulations. R.H. built and analyzed the reservoir model. T.Y. R.H. built the scanning optogenetics system. Y.I. supervised the project. R.H. wrote the paper with the comments of all authors.

Abstract

The cerebral cortex, cerebellum and basal ganglia are essential for flexible learning in mammals. Although traditionally thought to operate under different learning rules, recent evidence suggests that both the basal ganglia and the cerebellum may employ reinforcement learning mechanisms. This raises the question of how these structures coordinate when a common reward prediction error mechanism is active. To address this issue, we first examined output signals from the basal ganglia and cerebellum following the activity of the cerebral cortex. We recorded single-neuron activity from the output regions of the cerebellum and basal ganglia - the cerebellar nuclei (CN) and substantia nigra pars reticulata (SNr) - in both male and female ChR2 transgenic rats. Neurons in the CN and SNr exhibited distinct temporal response patterns; notably, the fast excitatory response in the CN, driven by mossy fiber input, was synchronized with the inhibitory response in the SNr, mediated via the direct pathway. Using these experimental findings together with connectome data, we developed both a semi-realistic spiking network model and a reservoir-based reinforcement learning model. In the latter model, successful learning depended on synaptic plasticity in both the cerebellum and basal ganglia with a temporal precision on the order of 10 ms. Furthermore, cortical β-oscillations enhanced learning and optimal reinforcement learning occurred when the output of cerebellar and basal ganglia signal phase-locked at the frequency of cortical oscillation. Taken together, our results suggest that the coordinated output of the cerebellum and basal ganglia, driven by tightly tuned cortical input, underlies brain-wide synergistic reinforcement learning.

Significance Statement

The cerebral cortex, cerebellum, and basal ganglia support learning. Recent research suggests that both the basal ganglia and cerebellum use a similar learning process called reinforcement learning, which involves predicting rewards. To understand how these brain regions work together, we recorded brain activity in rats while photo-stimulating the cerebral cortex. We found that two types of responses in the cerebellum and basal ganglia were synchronized, which might help activate the cerebral cortex. A computer model showed that precise timing of signals from both the cerebellum and basal ganglia is important for learning. This timing was important only when the cerebral cortex worked in a specific frequency range. Our findings suggest that coordinated brain activity enhances learning.

Introduction

The brain is a complex system composed of many unique information-processing regions that operate in a coordinated manner to produce flexible and sophisticated behavior (Caligiore et al. 2019; Doya 2000; Caligiore et al. 2017; Lake et al. 2017; Penhune and Steele 2012; Shadmehr and Krakauer 2008). To understand the mechanism of cooperative information processing, it is necessary to elucidate how the multiple interregional loop circuits work together. The cerebral cortex outputs to numerous subcortical structures, including the cerebellum and basal ganglia. These regions differ in many evolutionary and functional aspects but are similar in the fact that they send signals back to the cerebral cortex via the thalamus (Grillner 2021; Kebschull et al. 2020; Allen and Tsukahara 1974; Alexander and Crutcher 1990; Schell and Strick 1984). These multi-synaptic pathways, each with its own specific microcircuits and integration strategies, substantially affect ongoing activity of the cerebral cortex and entire brain.

Cerebellar nuclei (CN) are the output nuclei of the cerebellum and have direct thalamic projections, receiving inhibitory inputs from Purkinje cells (PCs), which are activated by excitatory granule cells that receive excitatory mossy fiber (MF) inputs. MFs are activated directly from the cerebral cortex, and consequently many neurons in CN receive inhibitory inputs from the cerebral cortex. MFs also directly excite CN neurons (Sugihara, Wu, and Shinoda 1996; Shinoda et al. 1992). Thus, CN receive multi-phase excitatory and inhibitory input from the cerebral cortex. The substantia nigra pars reticulata (SNr), an output nucleus of basal ganglia, is composed of inhibitory neurons projecting to the thalamus. In the SNr, a triphasic response to cerebral cortex stimulation in the order of excitation, inhibition, and excitation has been characterized in detail (Nambu et al. 2000; Chiken, Shashidharan, and Nambu 2008). To understand how these responses with excitatory and inhibitory dynamics are reintegrated in the thalamus and cerebral cortex, the relationships between multiple cerebral cortex areas and the subdivisions within cerebellum and basal ganglia should be systematically examined under identical conditions.

Coordination of cerebro-cerebellar loop plays an important role in cognitive and motor tasks (Wagner et al. 2019; Proville et al. 2014; Chabrol, Blot, and Mrsic-Flogel 2019; Gao et al. 2018; Zhu et al. 2023). Coordination of cerebro-basal ganglia thalamocortical loop is also critical in normal behavior and in pathological conditions (Wang et al. 2021; Alexander, DeLong, and Strick 1986; Yoshizawa et al. 2023; Stein and Bar-Gad 2013; Yasoshima et al. 2005; Alexander and Crutcher 1990). Classically, the basal ganglia and cerebellum were thought to be responsible for reinforcement and supervised learning, respectively (Doya 1999). However, the cerebellum has recently been shown to be also capable of reinforcement learning, as complex spikes in PCs are associated with reward prediction errors (Sendhilnathan et al. 2020; Yamazaki and Lennon 2019; Kostadinov and Häusser 2022; Thoma et al. 2008; Heffley and Hull 2019; Hoang et al. 2023; Boven et al. 2023; Pemberton, Chadderton, and Costa 2022). Thus, plastic changes in parallel fiber input in PCs due to climbing fibers input and plastic changes in corticostriatal pathways due to dopamine release could both lead to reinforcement learning. As circuit changes generated by different mechanisms facilitate learning, they must be consistently reintegrated in the cerebral cortex via the thalamus for decision making and motor output.

The cerebellum and basal ganglia each exhibit unique oscillatory activities (Halje et al. 2019; Courtemanche, Robinson, and Aponte 2013). For example, cerebellar oscillations in the β band range (15–30 Hz) is crucial for regulating action timing in human (Spencer and Ivry 2021). γ oscillations (30–80 Hz) can be also generated by cerebellar cortical circuitry (Middleton et al. 2008). β oscillation is simultaneously enhanced in cerebral cortex and basal ganglia when determining

motor output in rats (Leventhal et al. 2012). In motor cortex and basal ganglia, the β band oscillation is enhanced during reaching, grasping and other motor tasks (Khanna and Carmena 2015). The excessive β oscillation is observed in patients of Parkinson's disease (Gambosi et al. 2024; Morén et al. 2019). Thus, both the cerebellum and basal ganglia exhibit oscillations in the β-γ range, and their proper timing and amplitude are essential for behavioral coordination. The close frequency band activity of the cerebellum and basal ganglia may contribute to the coordinated information processing of the entire brain (Tanaka, Kameda, and Okada 2024; Diedrichsen, Ivry, and Pressing 2003; Petter et al. 2016).

In this study, we investigated the propagation of neural activity patterns of the cerebellum and basal ganglia in response to cerebral cortex photoactivation using high-throughput optogenetic stimulation (Hira et al. 2013; Hira et al. 2015; Hira et al. 2009; Sugino et al., 2024) and neuronal activity recordings with the high-density Neuropixels probes (Jun et al. 2017). Although the temporal response patterns differed, CN excitatory signals and SNr disinhibitory signals were synchronously elevated. We modeled these circuits with a spiking neuronal network based on connectome data and a reservoir-based reinforcement learning model and analyzed these synergistic features. The results indicate that the synergy can facilitate brain-wide consistent reinforcement learning.

Materials and Methods

Animal preparation

All experiments were approved by the Animal Research Ethics Committee of the Institutional Animal Care and Use Committee of Tokyo Medical and Dental University (A2019-274) and were carried out in accordance with the Fundamental Guidelines for Proper Conduct of Animal Experiment and Related Activities in Academic Research Institutions (Ministry of Education, Culture, Sports, Science and Technology of Japan). We used 17 adult male and female rats (Thy1.2-ChR2-Venus transgenic rats, Long–Evans strain (Tomita et al. 2009; Saiki et al. 2018) at the age of 10-29 weeks for cerebellar recording and 10-14 weeks for SNr recording. These rats were kept under an inverted light schedule (lights off at 12 AM; lights on at 12 PM) in their home cages to adapt to experimental surroundings.

Surgery

Primary surgery was performed to attach a custom-made head-plate (**Fig. 2C**) to the skull of rats under anesthesia by isoflurane gas (4.0–4.5% for induction and 2.0–2.5% for maintenance, Pfizer Japan, Tokyo, Japan) using an inhalation anesthesia apparatus (Univentor 400 anesthesia unit, Univentor, Zejtun, Malta). The body temperature was maintained at 37.0°C using an animal warmer (BWT-100, Bio Research Center, Aichi, Japan). The head of rats was fixed on a stereotaxic frame (SR-10R-HT, Narishige) with ear bars, and applied with lidocaine (Xylocaine Jelly, Aspen Japan, Tokyo, Japan) for local skin anesthesia and povidone-iodine disinfectant solution (10%, Kaneichi, Osaka, Japan) for disinfection around surgical incisions. The head-plate was then glued to the skull with stainless steel screws and dental resin cement (Super-Bond C & B, Sun Medical, Shiga, Japan; Unifast II, GC Corp., Tokyo, Japan). Reference and ground electrodes (PFA-coated silver wires, A-M systems, WA; 125-mm diameter) were implemented under the bone on the cerebellum. When we recorded the neurons in cerebellum, the reference electrode was placed over the anterior-most part of the cerebellum to avoid interference. Analgesics and antibiotics (meloxicam, 1 mg/kg sc, Boehringer Ingelheim, Tokyo, Japan; gentamicin ointment, 0.1% us. ext., MSD, Tokyo, Japan) were finally applied to remove pain and prevent infection.

More than three days later, secondary surgery was performed under the isoflurane anesthesia. For insertion of recording electrodes, we made a cranial window onto the cerebral cortex of left or right hemisphere or onto the cerebellum of the right hemisphere. The bone and dura mater were opened and removed by a dental drill (Tas-35LX, Shofu, Kyoto, Japan) and a dura picker (DP-T560-80, Bio Research Center, Aichi, Japan). The cortical surfaces were washed with PBS containing antibiotic (0.2% amikacin sulfate, Sawai, Osaka, Japan). We thinned the skull over the dorsal cerebral cortex and applied silicone oil to keep transparency for optogenetic stimulation (**Fig. 1F**). Thinned-skull area covered M1, M2, S1, and PPC. Because barrel cortex was not always completely covered with the thinned-skull window, we excluded the barrel cortex from S1 for the analysis when comparing the responsiveness. Analgesics (meloxicam, 1 mg/kg sc, Boehringer Ingelheim, Tokyo, Japan) was applied to remove pain.

Histology

After all recording sessions, the rats were perfused transcardially with saline and subsequent 4% formaldehyde in 0.1 M phosphate buffer under deep anesthesia with urethane (3 g/kg, ip, Nacalai Tesque, Kyoto, Japan) The brains were removed and then post-fixed with the same fixative for at least 12 h at 4° Celsius. The brains were removed and post-fixed with the same fixative for >2 days.

The brains were then embedded in 2 % agar in PBS and cut into sagittal sections with a thickness of 50 μm using a microslicer (VT1000S, Leica, Wetzlar, Germany). The serial sections were cover-slipped with mounting medium (DAPI Fluoromount-G, Southern Biotech, AL, USA). DiI, Venus, and DAPI (or NeuroTrace 435/455) were visualized through a fluorescence microscope (IX83 inverted microscope, Olympus, Tokyo, Japan).

Tracer study

Adult Thy1.2-ChR2-Venus transgenic rats (n = 6, male: 2, female: 4, 180-400 g) were used in this experiment. The rats were anesthetized with 2.5% isoflurane and an air flow of 0.2 liter per minute. Injection of AAVretro-CAG-tdTomato (Tervo et al. 2016) (addgene, Plasmid #59462-AAVrg, 2.4×10^{12} GC/ml, 0.2 μL, 0.02 μL/min or 0.5 μL, 0.05 μL/min, 10 min) were performed (Hamilton, 10 μL Microliter Syringe Model #801 RN) at the VL (n=3, 1.7 mm left lateral to midline, 2.3 mm posterior to bregma, and 5.8-6.1mm deep from the brain surface), VM (n=2, 1.4 mm left lateral to midline, 2.4 mm posterior to bregma, and 6.9 mm deep from brain surface), or VA complex (n=1, 1.6 mm left lateral to midline, 1.7 mm posterior to bregma, and 6.0 mm deep from the brain surface) of thalamus by pressure through a glass micro pipette. Two weeks after AAV injection, the rats were anesthetized with urethane, and then perfused intracardially with saline and fixative solution containing 4 % paraformaldehyde. The Brain was quickly removed and fixed in 4% paraformaldehyde for 2 days at 4 °C then placed in a 30% sucrose in PBS solution for several days until they sank to the bottom of their container. The brain was then immediately immersed in isopentane over dry ice then stored at −80 °C until sectioned. Sagittal sections (20 μm or 50 μm) were obtained in a cryostat (NX50, Epredia) at -20□ through the cerebellar nuclei, SNr and thalamus.

Optogenetics

We simulated and assembled a scanning optical system with galvanometer mirrors (6210H, Cambridge Technology, USA) to systematically and rapidly photostimulate many areas of the cerebral cortex (**Fig. 1A-E**). Simulation of optical pathway was made with OpticStudio (version16.5, Zemax, USA) to illuminate an area of 10 mm × 10 mm, more than 150 mm away from the objective lens. This allowed us to put the electrode at the space between objective lens and the brain. After validation in the simulation environment, we built up scanning light pathway with SM2-based cage system (Thorlabs, USA) and the multifunction I/O device, USB-6259 (National Instruments, USA). Scan lens (EFL = 39 mm, LSM03-VIS, Thorlabs) and tube lens (two achromatic doublets (f = 400 mm, ACT508-400-A, Thorlabs) placed in a Plössl design) made an infinity-corrected laser light beam into the pupil of objective lens. We put a plano-concave lens (f = – 150 mm, LC1611-A, Thorlabs) just above the camera lens (Nikon, f=105 mm) to extend the working distance. We kept the diameter of the laser at pupil small enough (<0.1 mm) for achieving a large PSF extension in the Z-axis at each stimulus point. This minimized the light density shift due to the curvature of the rat cerebrum and at the same time reduce the light spreading conically inside the brain, thus creating a columnar illumination. For functional mapping of cerebral cortex, we stimulated 32 × 32 grid (323 μm spacing, total 1,024 points) with 115 ms interval pseudo-randomly for 15 cycles (Hira et al. 2009; Hira, Ohkubo, Tanaka, et al. 2013; Hira et al. 2015; Hira, Ohkubo, Ozawa, et al. 2013). The stimulation point after the thin-skull point was always at bone, so that the stimulation interval of cerebral cortex was more than 230 ms. For functional mapping of cerebellum, we stimulated 32 × 32 grid (129 μm spacing, total 1,024 points) with 230 ms interval pseudo-randomly for 15 cycles. Recording during the stimulation at the bone was monitored as an internal control to distinguish any

contamination, including the neuronal activity responses to retinal light. We confirmed that there was no contamination of visually evoked activity in the responsive neurons that we analyzed. Each stimulation was 5 ms duration with 445 nm TTL-controllable diode laser (JUNO, Kyocera SOC, Japan). Laser power was set in each experiment sufficiently small not to induce movement when primary motor cortex was stimulated (0.7 mW–3.9 mW for stimulation of cerebrum, 15–21 mW for stimulation of cerebellum, at the center of field-of-view). Multi-unit activity (MUA) maps for varying laser power (**Extended Data 1 A-C)** indicated that the laser power we used was near the threshold at which evoked activity can be visualized. We also confirmed that the latency of the response and the shape of the map did not change significantly when we employed laser power that was strong enough to produce movement output. Even at the edge of the field of view (7.1 mm from the center), the laser power was >85.7% of the center. All system was controlled with custom-made software written with LabVIEW (National instruments, USA).

Electrophysiology

We performed electrophysiological recordings following the methodology described in our previous report (Sugino et al. 2024). Right before the recording, the Neuropixels probes (Jun et al. 2017) (IMEC, Belgium) were manually coated with lipophilic dyes, DiI (DiIC18(3), PromoKine, Heidelberg, Germany). The probes were fixed to a holder and handled using a micromanipulator (SM-15M, Narishige, Japan). Reference and ground electrodes were soldered, and attached to a custom-made part with four independent silver wires located under the skull onto the cerebellum. The probe was lowered in the coronal plane at 5–10 degrees from vertical at a speed of 10 μm/s until 8 mm below pia for recordings of SNr, thalamus, striatum and cerebral cortex, and at 30–63 degrees from vertical at a speed of 10 μm/s until 8 mm below the dura for recordings of cerebellum. They were left to settle for more than 30 min to reduce subsequent drift due to post-insertion brain relaxation. Recording was controlled with Open Ephys software (version 0.5, https://github.com/open-ephys/plugin-GUI/releases) (Siegle et al. 2017). Spiking activity and local field potential (LFP) were obtained at 30,000 samples/s and 2,500 sample/s, respectively after 500 Hz high-pass filtering and band-pass filtering with 0.5 – 1kHz range, respectively. We recorded the timing and location of photostimulation at the same time with USB-6001 (National instruments, USA) to align timing of each photostimulation with the neural signals. When the Neuropixel probe was placed to penetrate the cerebellar nuclei, a “bird sign” appeared on the LFP correlation structure (**Fig. 2A**). Histological observation revealed that the presence of this bird mark corresponded to the CN. The wing of the bird would reflect the fact that similar LFP signal appeared from white matter around the CN so that the correlation between the white matters is high, while the CN has specific signal, reducing the correlation between CN and white matter. We finally determined location of each channel at the level of the subdivision within CN or SNr by histological observations.

We recorded neurons from lateral and interposed nucleus of CN. These regions are known to preferentially interact with the motor cortex (Harvey, Porter, and Rawson 1979; Mushiake and Strick 1993; Ohmae, Kunimatsu, and Tanaka 2017; Thach, Goodkin, and Keating 1992). We recorded neurons evenly from the SNr. We focused on the ML axis for the analysis because striato-SNr projection across AP axis seems to be similar (Lee, Wang, and Sabatini 2020), and both received the dorsomedial or dorsolateral striatal input where motor cortex sends the projections.

Analysis of electrophysiological data

All analyses were performed with MATLAB (R2020a, Mathworks) or Python (version 3.7). Spike sorting was performed using KiloSort3 (https://github.com/MouseLand/Kilosort). Sorted clusters

were manually curated with Phy template GUI (https://github.com/cortex-lab/phy). The spontaneous firing rate of each neuron was obtained by averaging the firing rates for 50 ms before photostimulation.

For the cerebellar recordings, we determined the cell types of the curated neurons in the following way. First, we identified each neuron's region based on the LFP correlation structure described above. In the granule layer, we observed spiking activities with a NAW (negative after wave). Based on similar descriptions in rodents and monkeys (Beau et al. 2024; Muzzu et al. 2018; Prsa et al. 2009; Van Dijck et al. 2013; Van Kan, Gibson, and Houk 1993), we classified them as MFs. The complex spike of PCs was classified by a characteristic complex waveform and low firing rate (< 10 Hz) and the simple spike of PCs was identified according to recording location and high firing rate (> 20 Hz) (Sedaghat-Nejad et al. 2022; Sedaghat-Nejad et al. 2021; Cheron et al. 2009). We did not compare simple and complex spikes from the same neurons because we did not obtain sufficient numbers of PCs with both simple and complex spikes.

To identify “responsive neurons” to cerebral cortex stimulation and “receptive fields” in each responsive neuron, we first extracted the candidate points that satisfied the following inequalities:

$$\left|\frac{X - mean[bone]}{std[bone]}\right| > 1.64,$$

where X is the mean firing rate of the neuron 0–50 ms after stimulation and [bone] indicates stimulation at the skull surface. Then, we excluded the candidate points surrounded with ≤ four candidate points among eight surrounding points. Finally, if any candidate point was surrounded by ≥ five candidate points among eight surrounding points, we defined the neuron and candidate points as responsive neuron and receptive fields, respectively. This criterion collects stimulated points that form a local cluster based on the fact that the distance between the points is smaller than the resolution of the stimulus. Among 10,000 randomly shuffled data, no data satisfied this criterion. We confirmed that it identified fewer neurons than those that were visually identifiable, which allowed us to limit our analysis to neurons that had responded unambiguously.

PSTHs were created by collecting the firing responses to the receptive fields from 50 ms before to 150 ms after photostimulation in each trial. The peak latency was obtained by finding a maximum or minimum value after convolving the PSTH with a Gaussian function with sigma of 3 ms. To examine onset latency, the value of convoluted PSTH at the time of stimulation and its maximum or minimum up to 50 ms after stimulation was standardized to 0 and 1, respectively. The time at which this value first exceeded 0.4 was determined to be the onset latency. To obtain the average responsive maps, we translated each map based on the position of bregma and angle of midline before averaging. K-means clustering was done by the MATLAB function “kmeans”. For each pair that was simultaneously recorded, a −50 ms to 50 ms cross-correlation range of spiking activity was calculated, and a significant interaction was defined when the peak was > 99.8% of the peak synchronization level calculated by shuffling spikes in the same window 1000 times. Among them, we visually inspected pair by pair to determine the putative monosynaptic interactions.

Simulation of a spiking neural network

We created a spiking neural network with the Izhikevich model (Izhikevich 2003, 2007) in the Brian2 simulator in Python. The time step was set at 0.1 ms. The simulation time unit was ms. The Izhikevich model is described as follows:

$$\frac{dv(t)}{dt} = 0.04v(t)^2 + 140 - u(t) + I(t),$$

$$\frac{du(t)}{dt} = a\,(bv(t) - u(t)),$$

where u is potassium channel conductance, v is membrane potential, a is the leak current of the potassium channel, b is the voltage dependence of the potassium channel, c is post-depolarization potential, and d is the opening of the potassium channel after firing. When v exceeded 15 mV, the neuron was regarded to have an action potential, and v and u were reset to c and $u + d$, respectively. We determined parameters $a, b, c,$ and d based on previous studies (Thibeault and Srinivasa 2013; Muddapu et al. 2019; Izhikevich 2007) (**Table 2**).

We set the network connectivity of basal ganglia in detail based on recent anatomical studies at the submodule level (Foster et al. 2021; Jeon et al. 2022; Hintiryan et al. 2016) (**Fig. 7-1**). Conversely, although recent studies have provided essential knowledge (Pisano et al. 2021; Kebschull et al. 2020; Wu et al. 2023), because of limited projectome data of the cerebro-cerebellar loop circuit at a subdivision level (for instance, at the level of the microzone (Sugihara et al. 2009)), we modeled only a part of the cerebellar network with known anatomical connections. The synaptic circuit between submodules was shown in **Fig. 7-1A**. The connection probability (p) was a value between 0.008 and 0.15 and was assumed to be random. This probability was determined from previous studies and the axon density and was determined to match the results of our electrophysiology experiments. The connection probability where there is no anatomical connection was zero. There were no recurrent connections between the same submodules except those explicitly shown in **Fig. 7-1A**. We set the conduction delay of each connection as shown in **Fig. 7-1**. The delay was the same across the same connection types, but we varied the delay in three parts of the cerebellar circuit, i.e. MF → Granule cell, PF → CN, and Granule cell → PC. The variations in the delay of the three connections were defined as follows.

MF → Granule cell: x^2×20 ms,

PF → CN: x^2×20 ms,

Granule cell → PC ：x^2×16 ms,

where x was a random value between 0 and 1 for each pair of neurons. Each synaptic input was delivered immediately after the delay time as a transient voltage step in the Izhikevich model. Conduction delay and synaptic weight parameters were determined in agreement with the results of our electrophysiological experiments based on previous studies. The simplified diagram combining all the simulated networks with connection probability, conduction delay, and synaptic weight is shown in **Fig. 7A**.

For simplicity, we did not consider the following aspects in our model: gap junction, specific waveform of complex spike, pose of simple spike after the complex spike, short-term synaptic plasticity, long-term synaptic plasticity of most neuron pairs, dendritic structure, dendritic spike, neuromodulator, glial cells, and vascular endothelium.

As an input from the cerebral cortex, we simulated a Poisson spike train as a spiking activity of association cortex (N = 600 neurons). The spontaneous firing rate was set to 10 Hz, and the firing rate after virtual optogenetic stimulation was set to 100 Hz (5 ms). Virtual optogenetic stimulation was administered 15 times during 3000 ms of stimulation at various intervals. By visualizing a PSTH of each subdivision or each region, we manually modified synaptic weight, connection probability, and conduction delay by referring to electrophysiological data obtained in this study. Note that although we searched a broad set of parameters, the overall connection diagram was not changed, indicating that the circuit is consistent with our anatomical knowledge. After determining the parameters, we ran the simulation for longer time periods (6000 ms including 20 -30 stimulations), which were repeated 5 times.

Reservoir based reinforcement learning model

The dynamics of the cerebral cortex were modeled as a reservoir circuit described as

$$\tau \frac{dx_i}{dt} = -x_i + \sum_{j=1}^{N} W_{ij}^{REC}\ r_j + W_i^{tone} y_{tone} + W_i^{reward} y_{reward} + I_i^{noise},$$

$$z_{HD}(t) = \sum_{i=1}^{N} W_i^{HD} \int_0^{t_0} f_{HD}(t)\, s_i(t-t')\, dt',$$
$$z_{D}(t) = \sum_{i=1}^{N} W_i^{D} \int_0^{t_0} f_{D}(t)\, s_i(t-t')\, dt',$$
$$z_{ID}(t) = \sum_{i=1}^{N} W_i^{ID} \int_0^{t_0} f_{ID}(t)\, s_i(t-t')\, dt',$$
$$z_{P1}(t) = \sum_{i=1}^{N} W_i^{P1} \int_0^{t_0} f_{P1}(t)\, s_i(t-t')\, dt',$$
$$z_{P2}(t) = \sum_{i=1}^{N} W_i^{P2} \int_0^{t_0} f_{P2}(t)\, s_i(t-t')\, dt',$$
$$z_{P3}(t) = \sum_{i=1}^{N} W_i^{P3} \int_0^{t_0} f_{P3}(t)\, s_i(t-t')\, dt',$$

where $r_i = tanh(x_i)$ represents the firing rate of the *i-th* recurrent unit $(i = 1, \ldots, N)$, $s_i = (r_i + 1)^2$, and the filter functions f_{HD}, f_D, f_{ID}, f_{P1}, f_{P2}, f_{P3} were defined by the double-exponential function fitted to the experimental data (**Fig. 8B**). Because output neurons in the cortex are excitatory, s_i limits the output of the reservoir to positive values. It can also mimic the distribution of the firing activity of cortical neurons by converting it to highly skewed activity. The reservoir network was simulated at the time step of 1 ms. The variable y_{tone} and y_{reward} represents the input of tone and reward, respectively (1 or 0). $N = 800$ is the number of units, and $\tau = 20\,ms$ is the unit time constant. Since many cerebral cortices, including posterior parietal cortex, secondary motor cortex, and sensory cortex in rodents have neurons that respond to tone cue and reward signals (Hira et al. 2023; Barthas and Kwan 2017; Lacefield et al. 2019), both were added to the reservoir as inputs. The recurrent connectivity is represented by the $N \times N$ sparce matrix W_{ij}^{REC} where the connection probability between units is $p = 0.14$, and the weight follows a Gaussian distribution with a mean of zero and a standard deviation of 0.189. The activity of the network was read out by z_{HD}, z_D, z_{ID}, z_{P1}, z_{P2}, and z_{P3} through the $1 \times N$ output connectivity matrix W_i^{HD}, W_i^{D}, W_i^{ID}, W_i^{P1}, W_i^{P2}, W_i^{P3}, with initial values determined by a Gaussian distribution with a mean of zero and a standard deviation of 0.02. Here, because we regarded phase 3 as a rebound of phase 2, W_i^{P3} was the same as W_i^{P2}. The input weight vectors W_i^{tone} and W_i^{reward} followed a Gaussian distribution with a mean of zero and a standard deviation of 5. The values of y_{tone} and y_{reward} were 0, except during a tone or reward, comprising a step with a duration of 50 ms and amplitude of 1. A noise current was included as a $N \times 1$ random vector, I_i^{noise}, defined with a Gaussian distribution with a mean of zero and a standard deviation of 0.001. Reservoir circuits were designed to mimic the complex dynamics of the cortex, not to optimally configure the state for reinforcement learning.

Our spiking neural network is at semi-realistic scale and has a relatively large number of neurons (2.4x10^5 total neurons). It took about 20 min, or about 400 times longer to run the 3 sec simulation (Mother board: Z690/D4, CPU Intel Core i9-12900K 16 cores 3.2GHz, RAM 128GB). If this were used directly as a reinforcement learning model, it would take 13,300 hours to simulate 100 iterations in 20 minutes, which is practically impossible. Therefore, the cortex was modeled as a reservoir network, and the outputs of the basal ganglia and cerebellum were modeled as linear filters based on experimental data. Note that it took about 98 minutes for 100 iterations of the 20-min reinforcement learning model in our environment. Under these conditions, 123 hours were needed to

obtain the data in Fig. 8J. Maass and colleagues (Chen, Scherr, and Maass 2022) have proposed a fast method for including plasticity at a scale comparable to that of our semi-realistic spiking neural network. They have successfully imposed learning equivalent to backprop on a large spiking neural network. We believe that semi-realistic spiking neural networks could be used to elucidate the learning mechanism of our model in the future by using an appropriate learning rule.

Reinforcement learning task

The agent received the tone cue and reward as inputs and determined whether to hold or pull the lever at each time step of 100 ms. When the agent held the lever for 1 s, the tone cue was presented. If the agent pulled the lever before holding the lever for 1s, the tone cue was not presented, and the agent needed to hold the lever for 1s for the next tone cue. The agent needed to pull the lever within 0.3 s after tone cue presentation to get the reward. If the agent did not pull the lever within 0.3 s, the agent did not get the reward and needed to hold the lever for 1 s to receive the next tone cue. We have shown that rats can learn this task quickly (within a day of training) (Kimura et al. 2012; Kimura et al. 2017; Kawabata et al. 2020; Yoshizawa et al. 2023; Saiki et al. 2018).

The agent determined whether to pull or hold the lever every 100 ms, by comparing the pull value (q_{pull}) and hold value (q_{hold}). We defined these values as follows:

$$q_{pull} = z_D + z_{P1} + z_{P3} \ ,$$

$$q_{hold} = z_{HD} + z_{ID} + z_{P2} \ .$$

Here, the excitatory and inhibitory effect on the thalamus was regarded as the pull value and hold value, respectively. If the sum of these activities integrated in M1 from the thalamus or in the brainstem circuits exceeded the motor threshold, the lever was pulled. Thus, with q_{pull} and q_{hold}, we defined the probability of pulling, P_{pull}, as follows:

$$P_{pull} = \left[\frac{1}{1 + \ exp\ (\beta\, q_{hold} - \ \beta\, q_{pull})} \ - cost\right],$$

where $[x]$ returns x if x is positive and 0 if x is zero or negative, β = 1.2 is inverse temperature, and cost = 0.45 is the bias parameter. Every 100 ms, the maximum value of this probability was calculated, and this value determined pull or hold. A pull at the appropriate time was rewarded; however, there was a time lag of 0.2 s between the decision to output the action and the reward. This time lag was broadly consistent with the experimental data.

Learning

This simple model assumed that synaptic plasticity does not occur within the reservoir but only affects the direct pathways and PFs. All the synaptic plasticity was based on RPE, δ_t, defined as follows:

$$\delta_t = reward(t) + \gamma Q' - Q \ ,$$

where the discount rate γ was set to a half-life of 3 s. Q and Q' are values of consecutive time steps (Note that the time step of learning is 100 ms) as follows:

$$Q = q_{hold}\ (t) - \ q_{pull}(t),$$

$$Q' = q_{hold}\ (t + 100) - \ q_{pull}(t + 100).$$

Synaptic weight was renewed every 1 s (10 behavioral steps). Under the default condition, synaptic changes were made to the direct pathway and phase 2 as follows:

$$dw_i^D = \alpha\ \delta_t s_i(t)\ ,$$

$$dw_i^{P2} = -\ \alpha\ \delta_t\ s_i(t)\ ,$$

where the learning rate was $\alpha = 0.0025$. This difference in timescale was employed because the timescale in which LTP actually occurs is slower than the timescale for coincidence detection at the synapse. Additionally, random synaptic fluctuations with a standard deviation of 0.001 were added, and each synaptic weight was divided by the sum of synaptic weights in the corresponding pathways according to homeostatic plasticity. As phase 3 activity in the cerebellar nuclei was likely to be a rebound of phase 2 activity, W_i^{P3} was changed in conjunction with W_i^{P2}.

Synaptic changes in the direct pathway and PF-PC pathway in the cerebellum correspond to the dopamine-dependent LTP in the corticostriatal synapse (Yagishita et al. 2014) and CF-dependent LTD in the PF-PC synapse, respectively, when RPE is positive. Negative RPE increases local ACh concentration (Chantranupong et al. 2023), and cholinergic input induces LTD in the D1-positive medium spiny neuron (Shen et al. 2015). PF-PC synapses undergo LTP when PCs only exhibit simple spikes without complex spikes (Hirano 1990). Accordingly, we allow for bidirectional plasticity in both direct and PF-PC pathways.

To investigate how this learning depends on the properties of this model, we ran the same simulations with different parameters as follows. For each of the six unit time constants of 5, 10, 20, 30, 40, and 50 ms, we ran with delays of 0, 10, 20, 30, 40, 50, 60, and 70 ms on the basal ganglia or cerebellar signals. For noise dependence, we ran it by adding Gaussian noise with standard deviations of 0, 1, 2, 5, 10, and 20 times the standard deviation of the reservoir's output signal. When examining oscillation dependence, the Unit time constant was fixed at 50 ms. For the oscillation frequency dependence, simulations were performed by adding sine waves of 10, 15, 20, 25, 30, 35, 40, 60, and 100 Hz (the magnitude of the oscillation was 1.25 times the standard deviation of the input current) to the input current to the Unit. For the magnitude of oscillations, simulations were performed with 20 Hz sine waves of magnitudes 0.1, 0.2, 0.5, 0.75, 1, 1.25, 1.5, 1.75, 2.5, and 4.2 times the standard deviation of the input current. For the delay time, 20 Hz sine waves (1.25 times the standard deviation of the input current for the magnitude of the oscillation) were run with delays of 0, 10, 20, 30, 40, 50, 60, 70, 80, and 90 ms for the signal in thein the basal ganglia or cerebellum.

The same simulation was repeated with the time step for action and value updates changed from 100 ms to 50 ms (**Extended Data 4L-N**). The probability of pulling the lever was set to 1/2, as 50 ms doubles the number of times per a decision has to be made. The discount rate was set to the square root of the original value due to the change in bin width. The learning rate, amplitude of reward, and inverse temperature were set to the same value because the amount of reward per unit time did not change.

Statistics

The Wilcoxon's rank-sum test and χ^2- test were used for pairwise comparisons. Data were expressed as mean±S.E.M in the experimental data, ±S.D. in the simulation data unless noted otherwise.

Results

Transcranial optogenetic stimulation of cerebral cortex and neuronal recordings in CN and SNr

To stimulate large cortical areas in a point-by-point manner and to make comparisons between stimulated areas, we used transgenic rats (Mitani et al. 2022; Saiki et al. 2018) densely expressing ChR2 under the Thy1.2 promoter in all layers of the cerebral cortex under head-fixed conditions in the awake state. We previously reported a method enabling photostimulation of ChR2-expressing neurons in mice with retained skulls (TOS, transcranial optogenetic stimulation) (Hira et al. 2009; Hira, Ohkubo, Ozawa, et al. 2013; Hira et al. 2015; Hira, Ohkubo, Tanaka, et al. 2013). For optical stimulation of the rat cerebral cortex, the area that can be stimulated must be expanded. Therefore, we simulated the optical pathway and constructed a system with a photostimulation area of 10 mm × 10 mm based on the simulation results (**Fig. 1A–E**). We confirmed that photostimulation with our new system was possible in the transgenic rats by maintaining the transparency of a thinned skull in one hemisphere of the dorsal cerebral cortex (**Fig. 1F–J**). To determine the resolution of photostimulation, we stimulated neurons in the cerebral cortex with a 445 nm laser and recorded the surrounding spiking activity. Spiking responses of < 2 ms latency were observed in neurons < 0.5 mm from the center of optical stimulation in the cerebral cortex (**Fig. 1K**), indicating that direct photostimulation occurred within 0.5 mm from the center of the photostimulation site.

We divided a 10 mm × 10 mm area including a thinned-skull portion into 32 × 32 points and illuminated each point with a focused blue laser for 5 ms (**Fig. 1F**). We recorded CN and SNr neural activity using Neuropixels probes (Jun et al. 2017). In total, 544 and 282 neurons were isolated in CN (9 rats, 23 sessions) and SNr (8 rats, 19 sessions), respectively. We examined the exact recording location of each channel with histological data and local field potential (LFP) correlation structures. We identified the location of all recorded neurons at the level of subdivision of each region or layer (interposed or lateral nuclei for CN, molecular layer, granule cell layer, PC layer, white matter for neurons in the cerebellar cortex, medial (< 2mm from midline) or lateral (≥2 mm from midline) portion for SNr,).

Responses of a representative neuron recorded at lateral CN are shown in **Fig. 1L,M**. We displayed the average firing rate between 0–50 ms from the stimulus at each point on a color scale (hereafter referred to as the response map, **Fig. 1L**). The response map indicated that the neuron received the input from the primary sensory cortex (S1), primary motor cortex (M1), and secondary motor cortex (M2). We called the stimulation points that significantly affected the firing rates of recorded neurons the “receptive field” of the neuron. A raster plot and peri-stimulus time histogram (PSTH) for the receptive field are shown in **Fig. 1M**. We performed this analysis on all neurons and identified responsive neurons that had receptive fields.

Two types of response classes in CN neurons

To identify CN neurons, DiI fluorescence dye was applied to the Neuropixels probes, and the probe trajectories were identified histologically (**Fig. 2A**). We used 384 electrodes every 20 mm to skip one recording site, so that the recordings were linear over 7.5 mm. LFP correlation analysis revealed multiple clusters, which corresponded well with the histological layer structure and nuclear boundaries. In particular, we found the bird sign of the LFP (***** in **Fig. 2A**) enabling us to separate CN from their surroundings (see Methods). This corresponds to the fact that CN are located in white matter and are highly correlated with signals from white matter.

We identified two representative CN response classes. A typical class 1 response was a strong inhibitory response followed by an excitatory response (**Fig. 2B**), whereas a typical class 2 response

was transient excitation (**Fig. 2C**). K-means clustering (K = 6) of z-scored temporal response patterns of all responsive CN captured these two clusters: clusters #1 and #2 for class 1, and clusters #3 and #4 for class 2 (**Fig. 2D**). In clusters #1 and #2 (class 1), the onset and peak latency of inhibitory responses were 13.1 ± 0.6 ms and 41.2 ± 3.3 ms, respectively, and the onset and peak latency of excitatory responses were 58.9 ± 3.2 ms and 94.6 ± 2.9 ms, respectively. Neurons with class 1 response accounted for 56.7% (72/127) of all neurons. In clusters #3 and #4 (class 2), the onset and peak latency of excitatory responses were 14.0 ± 0.7 ms and 23.9 ± 0.4 ms, respectively. The excitatory peak of class 2 responses was significantly faster than that of class 1 inhibitory responses ($p = 2.9 \times 10^{-12}$, Wilcoxon's rank-sum test). Neuron with class 2 response accounted for 30.7% (39/127) of all neurons. Thus, neurons with class 1 and class 2 responses cover the majority (87.4%, 111/127) of CN responsive neurons. Neuron with class 1 response had a higher spontaneous firing rate than the neuron with of class 2 response (37.9 ± 2.0 Hz vs. 27.6 ± 4.0 Hz, p = 0.0053, Wilcoxon's rank-sum test), suggesting that neurons with class 1 and 2 responses have distinct biophysical properties.

It is unclear whether neurons with class 1 and class 2 responses are two completely different groups of neurons or whether a single neuron has both properties. Notably, some neurons exhibited mixed responses of class 1 and class 2. A neuron that was classified as class 1 had a transient fast excitatory response resembling class 2 only when S1 was stimulated (**Fig. 2E–G**). In other words, the class 2 response pattern was added only in S1, on top of the inhibitory to excitatory response pattern typically observed in class 1. Another neuron that was classified as class 1 had a class 2-like fast transient excitatory response when M2 or S1 was stimulated (**Extended Data 1 D–F**). Thus, class 1 and 2 responses can merge within a single neuron. Distinct response patterns depending on the stimulation areas indicate that CN can integrate the activity of multiple cortical areas in a manner that reflects area-specific time series information.

Furthermore, it is unclear whether the different response patterns of class 1 and class 2 depended on the location of stimulation or recording. The class 1 excitatory and inhibitory responses and the class 2 excitatory responses were evoked by a wide area of M2, M1, and S1, with no clear differences (**Fig. 2H**). The receptive fields of class 1 inhibitory and class 2 excitatory responses had receptive fields of up to 4–5 mm^2, with no clear differences (**Fig. 2I**). By contrast, more class 1 responses were observed in the lateral nucleus than in the interposed nucleus ($p = 3.8 \times 10^{-3}$, χ^2-test), whereas more class 2 responses were observed in the interposed nucleus than in the lateral nucleus (p = 0.040, χ^2-test; **Fig. 2K**). Thus, CN response patterns depend more on the location of the recording than that of the stimulus.

Recordings of PCs and MFs explain responses of CN neurons

There are multiple possible pathways from the cerebral cortex to the CN, and the pathways through which neurons with class 1 and 2 responses are generated remain unclear. We measured the activity of two structures that enter CN: MFs and PCs. MFs exhibit characteristic short waveforms of axonal activity and negative after waves (NAW) (Beau et al. 2024; Muzzu et al. 2018; Prsa et al. 2009; Van Dijck et al. 2013; Van Kan, Gibson, and Houk 1993). We determined MFs by waveform features and the observed layer. Most MFs showed very fast transient excitatory responses to cortical stimulation (**Fig. 3A,B**). Inhibitory responses were observed in five MFs, whereas 87 MF excitatory responses had an onset and peak latency of 11.0 ± 0.5 ms and 21.4 ± 0.9 ms, respectively, which were significantly faster (by 3 ms and 2.5 ms) than those of class 2 CN (onset: $p = 7.0 \times 10^{-6}$; peak: $p = 3.0 \times 10^{-5}$, Wilcoxon's rank-sum test; **Fig. 3G**). These results are consistent with the idea that fast excitatory responses of class 2 CN were via MF input, which is also anatomically plausible.

PCs are characterized by simple spike (SS) and complex spike (CS). We analyzed these two types of spiking activity separately. All complex spikes showed transient activity with jitter in a very narrow range (**Fig. 3C,D**; onset latency, 15.0 ± 0.6 ms, range, 12–19 ms; peak latency, 23.4 ± 0.7 ms, range, 20–28 ms). Notably, the cortical areas that elicited complex activity were confined to a portion of frontal cortex (**Fig. 3D**, left), and S1 rarely evoked complex spikes. SSs showed broad responses compared with complex spikes (**Fig. 3E,F**). The onset and peak latency were 15.4 ± 1.7 ms and 35.3 ± 3.1 ms, respectively. These values are comparable to those of class 1 inhibitory responses of CN. Additionally, the duration of the excitatory responses was roughly similar to that of CN class 1 inhibitory responses. Interestingly, the mean SS response had a transient decrease of firing activity 20–46 ms after photostimulation. This is compatible if the CS, which has a peak latency of 23.4 ms, pauses the SS for approximately 20 ms. We also examined the cross-correlograms of three putative SSs and three CN neurons in simultaneous recordings and found monosynaptic inhibition from SSs of PCs to CN neurons with class 1 response (**Fig. 3H,I**). Furthermore, the maps of inhibitory responses of CN and the maps of SS excitation overlapped (**Fig. 3J**). Similar result was observed in the other rat (**Extended Data 1 G-I**). Thus, monosynaptic inhibition from SS to CN neuron with class 1 response may directly contribute to the strong suppression of CN neurons with class 1 response after photostimulation. We examined all responsive MF-CN pairs closely and found no significant MF-CF pairs in cross-correlograms. We also closely investigated activity propagation between complex spikes and CN pairs, the equivalent of nuclear-olivary connections, and found no such pairs. To investigate the propagation of information between these pairs, it will be necessary to use multi-shank electrodes with higher electrode density in the future.

As the broad excitation after inhibition in class 1 response was not caused by MFs or PCs, it was most likely due to rebound excitation (Hoebeek et al. 2010; Aizenman and Linden 1999). By contrast, we found a CN neuron whose excitation after inhibitory activity differed across cortical areas (**Fig. 3K–M**). This neuron exhibited an increased excitatory response after photostimulation of M1 (blue, purple) but not M2 (red) or S1 (orange). Thus, the responses can switch in a region-specific manner. In summary, class 1 excitatory responses appear to be a rebound; however, the underlying process is complex, and the cerebral cortex may use this excitation to transmit region-specific information. Taken together, we illustrated the circuitry for phase 1 (excitation of class 2 responses), phase 2 (inhibition of class 1 responses), and phase 3 (excitation of class 1 responses) (**Fig. 3N**).

Two types of response classes in SNr neurons

Next, we examined the pattern of transmission from the cerebral cortex to the SNr, an output nucleus of the basal ganglia. We histologically confirmed the recording location (**Fig. 4A**). We identified two types of response classes in SNr neurons. Typical neurons with class 1 responses showed a clear triphasic pattern similar to that of previous studies (**Fig. 4B**) (Fujimoto and Kita 1992; Nambu et al. 2000; Nambu, Tokuno, and Takada 2002; Sano et al. 2013; Kitano, Tanibuchi, and Jinnai 1998). The triphasic response consisted of an excitatory-inhibitory-excitatory activity sequence in which the third excitatory response was always larger than the first one, and the firing activity was often completely suppressed during the second inhibitory phase. We also found a monophasic excitatory response (class 2) (**Fig. 4C**). K-means clustering (K = 6) of z-scored temporal response patterns of all responsive SNr neurons roughly captured these two classes: clusters #1 and #2 for class 1, and clusters #3 and #4 for class 2 (**Fig. 4D**). Neurons with class 1 (24/56) and class 2 (25/56) responses cover the majority (87.5%, 49/56) of SNr neurons.

We further investigated whether neurons with class 1 and class 2 responses are two completely different groups of neurons or whether a single neuron has both properties. One neuron with a class 1 response showed the triphasic response only when the frontal area was stimulated but showed a monophasic excitatory response when more posterior cortical areas were stimulated (**Fig. 4E**). Another neuron also showed a mixed response; however, class 1 and 2 responses were induced by the posterior and anterior part of the receptive field, respectively (**Fig. 4F**). These data are consistent with the idea that SNr can integrate information from different cortical areas with distinct patterns of activity transmission.

Some neurons only showed a fast excitatory response that had similar time courses to the first excitatory response of the class 1 triphasic response (**Fig. 4G**), an inhibitory response similar to the second inhibitory phase of the triphasic response (**Fig. 4H**), and an inhibitory-excitatory response pattern similar to the second and third phases of the triphasic response (**Fig. 4I**). Thus, the activities of neurons in SNr were characterized as based on the triphasic response, of which parts were missing (Nambu et al. 2023).

We further examined the dependencies of the response patterns on the locations of stimulation and recording. The excitatory source areas for neurons with class 1 and 2 responses distributed over a wide area of M2, M1, and S1 (**Fig. 4J**). Cluster #1 neurons in SNr also received inhibitory input from wide cortical areas including M2, M1, and S1 (**Fig. 4K)**. In clusters #1, #2, and #3, the sizes of the excitatory and inhibitory receptive fields were 3–4 mm^2 and 1–2 mm^2, respectively (**Fig. 4L**), supporting the center-surround model (Nambu et al. 2000). By contrast, more triphasic or inhibition-excitation responses were observed in the lateral SNr (>2 mm lateral from bregma) than in the medial SNr ($p = 0.014$, χ^2-test; **Fig. 4M**). Thus, response patterns in SNr depend more on the location of the recording than the stimulus. Of note, the medial SNr may also receive more triphasic input from higher-order regions, such as the prefrontal cortex and orbitofrontal cortex (Maurice et al. 1999), which were not stimulated in our experiment.

We investigated what anatomical pathways each pathway is composed of. Cross-correlograms of SNr neurons showed rare inhibitory interactions (**Extended Data 2A**). However, this inhibition does not explain the pattern of cortical responses to stimuli. The lateral inhibition inside the SNr does not seem to be large enough to shape the response patterns to cortical input. Based on previous studies (Fujimoto and Kita 1992; Nambu et al. 2000; Nambu, Tokuno, and Takada 2002; Sano et al. 2013), our data is consistent with the following circuit. The hyperdirect pathway runs from the cerebral cortex to the subthalamic nucleus to the SNr and is composed of fast transient excitation. The direct pathway inhibits SNr via the striatum. The indirect pathway activates the SNr after the hyperdirect and direct pathway inputs. The direct pathway can disinhibit the thalamus and cortex and makes a positive feedback loop between the cerebral cortex and basal ganglia. The hyperdirect pathway and indirect pathway localize the direct pathway spatiotemporally, resulting in a feedback circuit in which the cerebral cortex is continuously gated by the SNr (**Extended Data 2B**).

Retrograde tracing experiment

To determine which thalamic nucleus the SNr or CN neurons at the location we recorded project to, we injected AAV-based retrograde tracer (Tervo et al. 2016) (AAVretro-CAG-tdTomato) into the thalamus of Thy-1 ChR2 transgenic rats (**Fig. 5A**). Injections into the VL resulted in many tdTomato-labeled neurons in the bilateral CN but only a few in SNr (**Fig. 5C–F**). Within CN, labeled neurons were observed in the medial, interposed, and lateral CN bilaterally, but was brighter in the contralateral than the ipsilateral CN. In the contralateral cerebellum, axons collateral of CN neurons in the white matter and granule cell layer were also clearly labeled (**Fig. 5G.H**). We also confirmed

tdTomato-positive neurons in layers 5 and 6 of the motor cortex (**Fig. 5I,J**). After injection of VM, tdTomato-labeled neurons were observed in the ipsilateral SNr at 2.1–2.6 mm lateral to the bregma (but not in the medial SNr) and in medial, interposed, and lateral CN bilaterally (**Fig. 5K–O**). After injection of VA, tdTomato-labeled neurons were observed in the ipsilateral SNr at 1.4–2.6 mm lateral to the bregma and in medial, interposed, and lateral CN bilaterally (**Fig. 5P–T**). In all cases, contralateral CN were more densely labeled than ipsilateral CN, whereas contralateral SNr was not labeled. These results indicate that the neural activity of the CN propagates to the VL, VA, and VM, and that the activity of the lateral SNr propagates to the VM and VA, which is largely consistent with previous studies (Kaneko 2013; Kuramoto et al. 2009; Gornati et al. 2018; Kuramoto et al. 2015).

Cerebellar output to the thalamus, motor cortex, and striatum

The cerebellum and basal ganglia have direct connections that do not involve the cortex via thalamus (Bostan and Strick 2018; Yoshida et al. 2022; Ichinohe, Mori, and Shoumura 2000). The excitatory response of the CN when stimulated by the cerebral cortex might be transmitted to the striatum via the thalamus with a short latency (Chen et al. 2014). To investigate the fast propagation of activity from the cerebellum to the basal ganglia, we conducted electrophysiological recordings of the CN, motor cortex, centrolateral (CL) and ventrolateral (VL) thalamic nuclei, dorsolateral striatum (DLS), and dorsomedial striatum (DMS) during cerebellar stimulation (**Fig. 6**). We analyzed the neurons significantly increased the firing rate within 10 ms after photostimulation. Oblique laser incidence from behind the cerebellum through the transparent skull produced a very fast latency response (< 10 ms) in response to photostimulation (3.3 ± 0.40 ms, 8/37 neurons) (**Fig. 6G-I**). We confirmed that the CN neurons of the same transgenic rats express ChR2. The area where this response was detected covered the size of the CN (**Fig. 6G**), indicating direct stimulation of ChR2 on the soma or axons extending into the cerebellar cortex (**Fig. 5E**). We found evoked activity with a latency of < 10 ms in the VL (**Fig. 6J-L**; 5.0 ± 0.11 ms), CL (**Fig. 6M-O**; 5.4 ± 0.27 ms), motor cortex (**Fig. 6P-R**; 5.6 ± 0.27 ms) and striatum (**Fig. 6S-U**; 5.1 ± 0.40 ms; DLS or DMS). This indicates that the fast latency activity in DLS and DMS could be caused through the CN-thalamus-striatum pathway without going through the motor cortex. However, only 4.8% (6/126) of DLS and 4.1% (7/172) of DMS neurons responded to CN stimulation with a latency of < 10 ms, indicating that this CN-to-striatum activity propagation occurred only in a limited number of neurons. In fact, > 100 ms long-lasting activity was not often observed in SNr but in CN upon cerebral cortex stimulation. Thus, although this pathway has important functions in many aspects (Yoshida et al. 2022; Ichinohe, Mori, and Shoumura 2000; Alexander, DeLong, and Strick 1986), we will not consider it in the present study.

Hypothesis on brain-wide temporal integration

As CN→thalamus is excitatory and SNr→thalamus is inhibitory, increases in CN activity and decreases in SNr activity positively affect the thalamus. Notably, the excitation of class 2 response and the transient inhibition of the second phase of class 1 SNr response should coincidently activate the thalamus, as both of them two occur 20–30 ms after cortical stimulation (CN, **Fig 2D;** SNr, **Fig 4D**). Moreover, these two receptive fields almost overlapped (**Fig. 2I; Fig. 4J**). Therefore, a few tens of ms after the activity of a particular cortical area, signals that have passed through the SNr and CN circuits feedback synchronously to the cerebral cortex via the thalamus. We hypothesized that this synchronous positive feedback is the key to understand the brain-wide dynamics and learning. How the influence returns to the thalamus and cortex via the cerebellum and basal ganglia cannot be clarified experimentally because it is expected to be obscured by the mixture of various signals in the

thalamus. Accordingly, in the next section, we performed computer simulations to investigate how this brain-wide synchronous circuit works in a coordinated manner.

Spiking neural network reproducing representative activity of CN and SNr

Next, to investigate whether the activity propagation through these six pathways aligns with connectome data, we constructed spiking networks for the basal ganglia and cerebellum (**Fig. 7A,B; Fig. 7-1A; Table 2**). For the basal ganglia, we built a spiking neural network based on the connectome data using the Izhikevich model (Izhikevich 2003) (**Fig. 7-1B;** see **Methods**). This network contained the striatum, subthalamic nucleus, external globus pallidus, SNr, and thalamus (VL, VM, and parafascicular nucleus (PF)). The model reproduced a triphasic response to cerebral cortical stimulation in SNr neurons. To estimate which pathways from the cerebral cortex to SNr contribute to each phase of the triphasic response, we conducted virtual blocking experiments of synaptic connections (**Fig. 7C**). Blocking the hyperdirect pathway (i.e., monosynaptic input to the subthalamic nucleus from the cerebral cortex) eliminated the initial short excitatory response. Blocking the direct pathway abolished the second phase and weakened the third phase. Blocking the indirect pathway weakened the third phase.

Regarding the relationship between the cerebral cortex and cerebellum, it has been reported that the topography of the cortex is maintained particularly in the outputs from the pontine nuclei (Wu et al. 2023). However, this topography may be largely disrupted from granule cells to PCs (Pisano et al. 2021). Therefore, instead of creating a network model at a submodule level equivalent to that of the basal ganglia, we created a single module model for the cerebellum. We constructed a simulation consisting of MFs, granule cells, neurons in inferior olive, molecular layer interneurons, Golgi cells, PCs, and CN (**Fig. 7A,B; Table 2**). This model replicated the activity of class 1 and class 2 responses in CN (**Fig. 7D**). We conducted virtual blocking experiments as well. By blocking the projections from pontine nuclei to CN, only class 2 transient excitatory responses were eliminated. Blocking the synaptic functions from PCs to CN abolished class 1 responses. Therefore, CN neurons with class 1 inhibitory responses were inhibited by the PCs and then rebounded after inhibition in this model. Overall, our simulation replicated our electrophysiological results based on our current understanding of rodent brain circuits.

Integration of two loop circuits during ongoing activity

To examine how the CN and SNr responses merged, we added projections from CN and SNr to the thalamus. Based on the results of tracer experiments, we assumed that VM receives both inputs from SNr and CN, while VL only received input from CN. We also assumed here that these thalamic neurons do not receive direct input from cerebral cortex. Approximately 30 ms after photostimulation, both thalamic activities were elevated (**Fig. 7E**). VL showed second peak of activity. To investigate how these thalamic activities can merge in the cerebral cortex, we simulated layer 5 pyramidal neuron (L5PN) receiving both inputs (Kaneko 2013; Hooks et al. 2013). Again, we assumed that this neuron does not receive input from surrounding cortical neurons. The L5PN showed triphasic responses, where the first excitatory signal was the summation of the direct pathway and CN phase 1 activities, the second inhibitory signal was the summation of the indirect pathway and CN phase 2 activities, and the third excitatory signal was CN phase 3. To investigate whether the synchronization of direct pathway and MF-CN pathway plays a role in information integration, we changed the axon conduction time of either corticostriatal and cortico-subthalamic projections or corticopontine and cortico-olivary projections (**Fig. 7F,G**). The exact synchronization at the timescale of 10 ms enhanced the summation of the CN and SNr outputs at the L5PN

approximately 40 ms after the stimulation of cerebral cortex. Thus, our simulation reveals the importance of the temporal dynamics of outputs from the cerebellum and basal ganglia for information transmission back to the cerebral cortex via the thalamus. In the real brain, the interactions between thalamus and cortex that we have neglected would be complex. Synchronization of signals through the cerebellum and basal ganglia would be additive on top of such activity, thus controlling neurons in the cortex.

Reservoir-based reinforcement learning model

Finally, we examined how the interaction of cortico-cerebellar and cortico-basal ganglia circuits contributes to learning. Recent studies have shown that in addition to dopamine neurons in the basal ganglia, complex spikes in cerebellar PCs reflect reward prediction error (Sendhilnathan et al. 2020; Kostadinov and Häusser 2022; Hoang et al. 2023; Heffley and Hull 2019; Thoma et al. 2008). This indicates that reinforcement learning should progress in both the basal ganglia and cerebellum. Thus, we investigated how reinforcement learning, which progresses in these different systems, merges coherently.

We built a model in which the activity of the cerebral cortex was represented by a reservoir of 800 units with a time constant of 20 ms and that produced complex dynamics in response to an auditory cue and reward inputs (**Fig. 8A**). For the basal ganglia, we assumed that the output is the result of convolving cerebral cortex activity with pathway-specific filters in the hyperdirect, direct, and indirect pathways (**Fig. 8B**, left). Similarly, for the cerebellum, the output was assumed to be the result of convolving the reservoir output with filters corresponding to CN phases 1, 2, and 3 (**Fig. 8B**, right). These six filters were made to tightly reproduce the experimental data.

Using this circuit, we trained a simple reinforcement learning task (**Fig. 8C**). The agent had to pull or hold a lever to get a reward. When it held the lever for 1 s, the tone cue was presented. The agent had to pull the lever within 0.3 s after the tone cue to get a reward. The decision to pull or hold the lever was made by comparing the pull value and hold value. The pull value was defined as the sum of the output results from the direct pathway, phase 1, and phase 3, since the activity of these pathways would enhance thalamic and cortical circuits leading to the pull behavior. The hold value was defined as the sum of the output results from the hyperdirect pathway, indirect pathway, and phase 2. These values were converted to lever pull probability using a sigmoid function, and based on this, the decision to pull or hold was made every 0.1 s. As pulling the lever requires force, a bias term was added to the sigmoid function to make pulling less likely. The final behavioral output, determined by integrating the outputs of the basal ganglia and cerebellum, was assumed to occur in the M1 via the thalamus. Synaptic plasticity occurred based on reward prediction error on corticostriatal synapses of the direct pathway and PF-PC synapses. Positive and negative reward prediction error (RPE) induced LTP and LTD in corticostriatal synapses, respectively, and LTD and LTP in PF-PC synapses, respectively (see **Methods**).

The simulation results show that the agent increased the reward acquisition rate during a 20 min training period (**Fig. 8D**). To investigate which components of the model are critical for successful learning, we first blocked the plasticity of either the basal ganglia or the cerebellum. This significantly reduced the rate of reward acquisition in both cases, suggesting that plasticity of both structures is important for learning in this model (**Fig. 8E left**). We then blocked 50% of the signaling in each pathway (**Fig. 8E right**). The blockage of any pathway inhibited learning, but in particular blocking either direct pathway in the basal ganglia or phase 2 pathway in the cerebellum abolished learning. Conversely, blocking the hyperdirect pathway in the basal ganglia and phase 1 pathway in the cerebellum had a relatively limited effect. These findings indicate that two pathways

in which plasticity works play a particularly important role. Basal ganglia and cerebellar inputs contain independent components from other brain regions and periphery as well as cortical activity. We compared the number of rewards acquired in the early and late stages of learning by applying independent noise to the basal ganglia and cerebellar inputs. We found that learning was not impaired even when the standard deviation of the independent noise was twice the standard deviation of the signal from the cerebral cortex (**Extended Data 4A-C**). This indicates the robustness of the cooperation between the basal ganglia and the cerebellum.

During the learning process, the pull value increased and hold value decreased immediately after the sound, whereas the pull value decreased and hold value increased during the holding period. In accordance with this, 200 ms after the tone presentation, the activities of the striatal direct pathway and cerebellar phase 2 pathway increased and decreased, respectively (**Fig. 8F**), whereas 600 ms after the tone presentation, these changes were milder (**Fig. 8G**). Thus, synaptic plasticity of both pathways occurred in a coherent manner to induce efficient behavior. Note that this model predicts that the triphasic activity patterns in response to cerebral cortex activity change from early to late learning stages (**Fig. 8F,G**).

To investigate whether the precise timing of the outputs from the basal ganglia and cerebellum contributes to learning, we delayed the output timing of the basal ganglia or cerebellum (**Fig. 8H**). Notably, delaying the output of the basal ganglia or cerebellum by only 10 ms reduced the reward acquisition rate. The greater the delay (up to 70 ms), the lower the reward acquisition rate. These findings suggest that the mutual timing of responses from the basal ganglia and cerebellum, as observed in experimental data, is optimized for cooperative reinforcement learning between the two structures. Thus, we investigated how this time-delay effect relates to the time-scale of cerebral cortex activity. We varied the time constants of neurons in 5 or 10 ms steps (from 5 ms to 50 ms) (**Fig. 8I**). When the time constant of a neuron was 10 ms, 20 ms, or 30 ms, delay-dependency was observed (**Fig. 8J,K**). These results suggest that delay-dependency requires a β- to γ-range timescale of cerebral cortex activity.

To investigate the relationship between cortical oscillation frequency and learning, we inputted oscillations as currents to the neurons, which constitutes the reservoir. When a 20 Hz sine wave was inputted, the global dynamics were similar to those of a sine wave with an amplitude 1.25 times larger than the original standard deviation (**Extended Data 4D**). When the amplitude was varied, the number of rewards acquired in the early and late stages of learning was found to increase when oscillations of around 1.25 times the amplitude were given (**Extended Data 4E**). Furthermore, when the oscillation frequency was changed while maintaining the amplitude of the oscillation, it was found that this enhancement effect occurred only with β-oscillations (20-30 Hz), not with γ oscillations (40-100 Hz) (**Extended Data 4F, G**). Investigations of the time-delay effect showed that the number of reward acquisitions had 20-Hz oscillatory cycle, which indicate the successful learning depends on the coherence of cortical oscillation and sum of output from the basal ganglia and cerebellum (**Extended Data 4H**). These results indicate that the facilitation of oscillatory frequency-dependent learning in the cortex is due to phase synchronization of feedback signals from the basal ganglia and cerebellum at the dominant frequencies. These results indicate that phase synchronization of cortical β-oscillations with those of the basal ganglia and cerebellum contributes to consistent reinforcement learning, which is consistent with previous studies on β-oscillations in the mammalian brain (Igarashi et al. 2013; Popa, Spolidoro, et al. 2013; Stein and Bar-Gad 2013).

To investigate in more detail what properties of the response functions of the basal ganglia and cerebellum are responsible for the oscillatory frequency dependence of the cortex, we performed simulations by varying the time scale of the response functions (**Extended Data 4I**). When the

response function was shorter in time (0.8 times) than the real data, i.e. when the feedback of cortical activity occurred on a shorter time scale, the frequency dependence shifted towards higher. Conversely, when the response function was longer in time (1.5-fold) and earlier than the real data, the frequency dependence shifted towards lower. Furthermore, this frequency dependence of learning matched well with the frequency dependence of the power spectrum of the sum of the six response functions at the respective time scales (**Extended Data 4I, right**). This indicates that the oscillatory frequency-dependent facilitation of learning is contributed by the degree of agreement with the frequency of the feedback signals from the basal ganglia and the cerebellum. In addition, to investigate whether the results in **Extended Data 4H** could also be explained by the power spectrum, we examined the power spectral density of those summations when the response functions of the cerebellum or basal ganglia were delayed. The delay time dependence of the power spectral density at 20 Hz was in sharp agreement with delay-dependent learning (**Extended Data 4J**). In contrast, the power spectral densities at 10 Hz or 40 Hz were quite different. These results indicate that the facilitation of oscillatory frequency-dependent learning in the cortex is due to phase synchronization of feedback signals from the basal ganglia and cerebellum at the dominant frequencies.

Finally, to check whether the results of our reinforcement learning model were independent of the time step of the action, we changed the time step from 100 ms to 50 ms in our simulations. In line with this, we reduced the probability of pulling the lever in one decision by 1/2. This made the probability of pulling at 100 ms equal to the original probability. The results of blocking plasticity experiment, the time-delay dependence and the phase period dependence for the periodic input to the cortex were all qualitatively the same as for the 100 ms step (**Extended Data 4L-N**). Thus, our reinforcement learning model is robust irrespective of time step.

Discussion

In this study, we used optogenetics and electrophysiological recordings, which revealed that the response patterns of most single neurons in CN and SNr to cortical stimulation can be categorized into two classes. In CN, we observed inhibition followed by excitation (CN class 1) and transient excitation (CN class 2). In SNr, we observed a triphasic response (SNr class 1) and monophasic excitation (SNr class 2). The timescale of CN responses was slower than that of SNr responses. The effects on the thalamus in total were expected in the order of inhibition-excitation-inhibition in SNr and excitation-inhibition-excitation in CN. Notably, the MF-CN pathway of the cerebellum and the direct pathway of basal ganglia were synchronized. The response patterns could be reproduced by a spiking neural network model of basal ganglia and cerebellum based on currently available connectome data. We developed a model in which the cerebral cortex is the reservoir, and reward prediction error signal prompts LTP of striatal direct pathway neurons and LTD of parallel fiber synapses onto PCs. We found that cerebellar and basal ganglia dynamics aligned with experimental data with an accuracy of 10 ms facilitated cooperative reinforcement learning. Moreover, cortical β-oscillation was identified as critical for the successful learning. Overall, these data reveal a mechanism for the brain-wide synergy that underlies consistent reinforcement learning in the basal ganglia and cerebellum.

Previous computational studies have investigated the relationships among cerebral cortex, basal ganglia, and cerebellum (Houk and Wise 1995; Caligiore et al. 2019; Houk et al. 2007). However, our model with reinforcement learning is the first model based on realistic temporal response patterns of the cerebellum and basal ganglia in response to cerebral cortex activation. Our detailed analysis of temporal activity patterns revealed that β-range activity of the cerebral cortex enhances synergistic effects. Regarding oscillations, synergistic improvements were only observed for β-oscillations (20-30 Hz), not for γ-oscillations (40-100 Hz). The β-oscillation in the sensorimotor cortex has been observed during preparation and execution of voluntary movement (Stein and Bar-Gad 2013; Igarashi et al. 2013; Popa, Spolidoro, et al. 2013). Our model is also the first to assume that both the cerebellum and basal ganglia are engaged in reinforcement learning. Previously, it was assumed that the basal ganglia were responsible for reinforcement learning and the cerebellum for supervised learning, supposing a clear division of labor (Doya 2000, 1999). Our model proposes a novel mechanism of linking multiple plasticity events across distinct brain regions. That is, the synapses that are thought to most often undergo plastic changes in the basal ganglia and cerebellum are pathways that synchronously send back signals from the cerebral cortex. This parallel circuit can coincide by inducing plasticity on the direct pathway and PF-PC synapses, allowing reinforcement learning to proceed consistently.

Why does learning efficiency critically depend on cortical oscillation frequency and on the synergy of basal ganglia and cerebellar outputs at specific frequencies, even though our model simply assumes the summation of linear filters? Now, consider a parallel linear system with input and output time series $x(t)$ and $z(t)$ whose Fourier transforms are $X(f)$ and $Z(f)$, respectively, where t denotes time and f denotes frequency (**Extended Data 4K**). The input and output correspond to cortical activity and decision probability, respectively. Let the response functions, i.e. impulse functions, of the basal ganglia and cerebellum be $b(t)$ and $c(t)$, respectively, with corresponding Fourier transforms $B(f)$ and $C(f)$. The composite response function is given by $b(t) + c(t)$, and by linearity, its Fourier transform is $B(f) + C(f)$. The analysis regarding cortical oscillation suggested a close relationship between learning efficiency and the power spectrum of the output. This power spectrum $|Z(f)|^2$, which may be highly correlated with

learning efficiency, can be expressed as

$$|Z(f)|^2 = |B(f) + C(f)|^2 |X(f)|^2,$$

which expands to

$$(|B(f)|^2 + |C(f)|^2 + 2Re\{B(f)C(f)^*\}) |X(f)|^2$$

where $Re\{\}$ denotes the real part and * indicates complex conjugate. Frequency shifts in response filters shown in **Extended Data 4F,G,I** alter $|B(f)|^2$ and $|C(f)|^2$, potentially resulting in changes in learning efficiency. The cross term $2Re\{B(f)C(f)^*\}$ depends on the phase difference between the response functions of basal ganglia and cerebellum, reaching a maximum when they are in phase and a minimum when they are in antiphase. This explains the time-delay dependency analyzed in **Extended Data 4H,J.** Moreover, the phase synchrony at the frequency of cortical oscillation, which could enhance $2Re\{B(f)C(f)^*\}) |X(f)|^2$, is consistent with **Extended Data 4I.** The close relationship between output power spectral density and learning efficiency may be due to the fact that a higher spectral density provides a broader dynamic range for synaptic plasticity to adjust the context-dependent modulation of behavioral outputs, thereby enabling robust learning. Therefore, during the learning process, to enhance the output power spectrum in the β band, the outputs of the basal ganglia and cerebellum may tend to become phase-locked at β-frequency range.

It is known that axons from VL and VM are distributed across the different layers of the cerebral cortex (Kaneko 2013). VM especially projects to apical dendrites in layer 1, whereas VL projects to the basal dendrites of L5 pyramidal neurons (Kuramoto et al. 2015). Synchronous inputs to tuft and proximal dendrites within 20 ms enhance nonlinear integration, leading to dendritic spikes and bursting (Ledergerber and Larkum 2012; Poirazi and Papoutsi 2020). In the motor cortex, cortico-spinal neurons may detect this coincidence and directly convert it into motor output. Thus, if cerebellar and basal ganglia outputs are synchronized with a precision of 20 ms, activity of VL and VM could facilitate strong motor output via dendritic spikes in the motor cortex. This necessary timescale is consistent with the timescale that we have identified to promote thalamic activity in simulation and coordinated reinforcement learning in our model (i.e. β-range). Dendritic spiking may also induce synaptic plasticity, and simultaneous active input from the cerebellum (Popa, Velayudhan, et al. 2013) and basal ganglia (Ueki et al. 2006) may facilitate circuit formation in the cerebral cortex. β band oscillation is found in the motor cortex, basal ganglia, and cerebellum (Courtemanche, Robinson, and Aponte 2013; Halje et al. 2019; Spencer and Ivry 2021; Middleton et al. 2008; Khanna and Carmena 2015; Morén et al. 2019; Igarashi et al. 2013; Leventhal et al. 2012). Taken together, we propose that the cerebellum, basal ganglia, and cortex acquire plasticity in a coordinated manner through β rhythm, resulting in consistent behavioral decisions and reinforcement learning throughout the brain.

Whether the mechanisms of consistent reinforcement learning that we modeled here explain the actual brain's learning principle remains to be tested. As shown in **Fig. 8F**, excitatory transmission from CN to the thalamus and inhibitory transmission from the SNr to the thalamus will be larger and smaller, respectively, upon execution of the reinforced behavior after learning. By contrast, these transmissions will be smaller and larger, respectively, if the behavior does not need to be executed (**Fig. 8G**). It should be noted that CN and SNr activity in response to non-specific activation of the cerebral cortex will not change during learning. It is necessary to artificially stimulate cortical neurons to induce or suppress the behavior to be reinforced to verify these predictions. Moreover, optogenetic inhibition of PCs (whose activity is suppressed during the stimulation of cortical neurons that are involved in reinforced behavior) and optogenetic activation of striatal neurons in the direct pathway (whose activity is increased during the stimulation of cortical neurons that are involved in reinforced behavior) would cause the execution of the reinforced behavior via the

thalamus and cerebral cortex. These experiments could be possible by combining an activity-dependent genetic switch (Wang et al. 2017; Lee et al. 2017), such as Cal-Light or FLARE (Lee et al. 2017; Wang et al. 2017) with tet-dependent. In addition, measuring the axonal activities from SNr and CN onto the thalamus during specific behavior would be useful. This could be done, for example, by expressing voltage sensor proteins with different fluorescence wavelengths in the SNr and CN and observing the thalamus through the GRIN lens. These axonal activities are predicted to be synchronized and phase-reversed in beta oscillations during the preparation or execution of a specific behavior.

We have found that CN responses are categorized into distinct class 1 and 2 activities. The excitatory inputs in class 2 were thought to be via MFs (Tsukahara, Korn, and Stone 1968; Hesslow, Svensson, and Ivarsson 1999; Wu, Sugihara, and Shinoda 1999); however, involvement via CFs (Sugihara, Wu, and Shinoda 1996) or disinhibition of PCs cannot be ruled out. Although many class 1 neurons did not show fast excitation, they can change to class 2 because MF-CN synapse potentiation can be induced by pairing with post-inhibitory rebound of CN neurons (Pugh and Raman 2008). As the MF-CN pathway is disynaptic, and the MF-granule cell-PC-CN pathway contains four synapses, the MF-CN pathway is considered faster. However, as indicated in **Fig. 2F** (* in the right panel), inhibition may precede excitation. Thus, even with signals starting simultaneously from the cerebral cortex, PCs may be able to alter the impact of the MF on the CN. CN phase 3 could represent post-inhibitory rebound excitation (Hoebeek et al. 2010; Aizenman and Linden 1999), excitation by internal circuits in CN, and reverberation by circuits not recorded in this study. A marked difference in the proportions of class 1 and class 2 in interposed and lateral CN could be due to the relative differences in MF and PC input. However, this requires further investigations in future studies.

Finally, we list below the limitations of this study and future directions. Convolution of the impulse response assumes a linear model; however, the brain is clearly not linear, and nonlinearities must be considered in many cases. We assessed the cerebellum and basal ganglia; nevertheless, other areas, such as the superior colliculus and sensory cortex, are also involved in decision making. We also disregarded the corticothalamic projection, even though the mechanisms by which inputs from the cerebral cortex merge with those from SNr and CN in the thalamus are most likely important. It is possible that rebound excitation of CN class 1 contributes to working memory maintained by the cerebro-cerebellar loop (Gao et al. 2018), which should be examined in the future. The mechanism by which the RPE is shared between the basal ganglia and cerebellum should also be clarified. As cooperation between the basal ganglia and cerebellum is important for facilitating learning throughout the brain, dysfunctions in one area may affect both areas. For example, diseases related to the basal ganglia, such as Parkinson's disease, obsessive-compulsive disorder, and Tourette's syndrome, may also be associated with the cerebellum as previously discussed (Bostan and Strick 2018; Caligiore et al. 2017; Li, Le, and Jankovic 2023). Thus, our findings may call for re-interpretation of various brain pathologies.

Figure legends

Figure 1. Optogenetic stimulation and electrophysiological recordings.
A. 3D CAD data for the system. **B.** Photographs of the system. WD, working distance. **C.** Four laser beams correspond to scanning angles of 0, 4, 8, and 12 degrees, which focus at distances of 0, 2.4, 4.7, and 7.1 mm from the center, respectively. The objective lens (Nikon camera lens) was substituted by a lens with the same focal length. **D.** Grid distortion of 32 × 32 stimulation points (10 mm × 10 mm). **E.** Proportion of encircled energy as a function of the distance from the centroid. **F.** A photograph of thinned skull preparation. The blue dots correspond to the point of photostimulation. The blue vertical and horizontal lines indicate the intact skull bone. **G.** Dorsal view of brain atlas of right hemisphere. The blue square represents the 10 mm × 10 mm stimulation area. The black dot denotes the bregma. **H.** Headplate design. **I.** Approximate positions of recording pass 0 (cerebral cortex), pass 1 (for cerebellar nuclei (CN)), and recording pass 2 (for substantia nigra pars reticulata (SNr)). **J.** A photograph from the top during photostimulation of the cerebral cortex and recording at the cerebellum. **K.** Spike latency map of a single neuron in the cerebral cortex showing the resolution of photostimulation. **L** A representative responsive map for a single CN neuron. The purple polygons indicate the receptive field of the neuron. **M**. A raster plot (top) and PSTH (bottom) for trials in which photostimulation was performed on the receptive field in **L.**

Figure 2. Two major classes of response patterns observed in cerebellar nuclei (CN) neurons.
A. A sagittal section of cerebellum in a ChR2-Venus transgenic rat (left) and local field potential (LFP) correlation structure of the corresponding animal recorded with Neuropixels (right). DiI fluorescence shows electrode location. Dotted lines indicating boundaries of LFP correlation structure correspond to histologically confirmed cerebellar layer structure and cerebellar nuclei. **B,C.** Response maps of typical class 1 (**B**) and 2 (**C**) responses in CN (left). Magenta frames indicate responsive pixels. Raster plots and PSTHs for the responsive pixels (right). **D.** Z-scored PSTH of all CN neurons clustered by K-means clustering (top) and mean PSTH of each cluster (bottom). Colors correspond to cluster numbers. The thickness indicates the numbers of neurons in the cluster. **E.** A map of the difference in firing rate at two time bins: −50–0 ms (A) and 20–30 ms (B) after stimulation of a CN neuron. **F.** Raster plots and PSTHs for the blue and red polygons in **E**. * indicates a transient inhibitory response before the fast excitatory response. **G.** An overlay of the PSTHs in **F**. **H.** Average input maps of class 1 neurons at 0–50 ms (left) and 50–200 ms (right) in CN. **I.** An average input map of a class 2 neuron in CN. **J.** Time course of excitatory and inhibitory responsive areas in clusters #1–4. K. The same analysis as **D**, but separated according to recording location. **Extended Data 1** is available for more basic analysis.

Extended Data 1. Cerebellar nuclei (CN) neuron responses.
A. Laser power dependence of response maps of multi-unit activity in the cerebellar nucleus. **B.** Laser power dependence of response latencies in the same recordings as in panel **A**. **C.** PSTH of the same multi-unit activity as in A during stimulation at 1.6 mW (top) and 7.2 mW (bottom). **D.** Maps of firing rates 30–50 ms (B) after stimulation (left) and the difference in firing rates (right) at two-time bins: 20–30 ms (A) and 30–50 ms (B). **E.** Raster plots and PSTHs for the stimulus points enclosed by the red, blue, and orange polygons in **D**. **F.** Overlaid PSTHs**. G.** Cross-correlogram of simultaneous recordings of a PC (SS) and a neuron in CN. **H.** Rater plot and PSTH of the presynaptic PC (SS) in **G. I.** Rater plot and PSTH of the postsynaptic CN neuron in **G.** PSTHs in **H** and **I** were generated in trials with photostimulation of the receptive field of the PC for comparison.

Figure 3. Activity propagation from the cerebral cortex to cerebellar nuclei (CN) neurons.
A,C,E. A response map, raster plot, and PSTH of a mossy fiber (MF) neuron (**A**) and complex spike (**C**) and simple spike (**E**) of a PC. **B,D,F.** Normalized average responses (left) of MF neurons (**B**) and complex spikes (**D**) and simple spikes (**F**) of PCs. The order was sorted by the peak time. Average maps of all activities (right). **G.** Mean firing rates of CN neurons with class 1 responses, CN neurons with class 2 responses, MFs, SS (simple spike), and CS (complex spike). Shaded areas indicate phases 1–3. **H.** Cross-correlogram of simultaneous recordings of three PCs (SS) and three neurons in CN. **I.** A predicted synaptic circuit among neurons in **H. J.** Response maps and PSTHs of six neurons shown in **H**. All PSTHs were generated in trials with photostimulation of the receptive field of the blue neuron (SS#0702060) for comparison. **K.** Firing rates 20–40 ms after photostimulation (A in **L**) of a CN neuron (left) are shown as a map. Firing rates 50–70 ms after photostimulation (B in **L**) minus that of A of the same neuron are shown

as a map (right). **L.** Raster plots and PSTHs of CN neurons from the color-corresponding areas specified in **K. M.** Mean firing rates of CN neurons from the color-corresponding areas in **K** when photostimulated**. N.** Possible pathways from the cerebral cortex to CN. Phases 1, 2, and 3 correspond to the time for excitatory input in class 1 response, inhibitory input in class 2 response, and excitatory input in class 2 response.

Figure 4. Analysis of single neuron response patterns of substantia nigra pars reticulata (SNr) to cortical stimulation.

A. A sagittal section showing electrode traces with DiI. **B.** A map, raster plot, and PSTH of a typical SNr neuron with class 1 response (a triphasic response). **C.** A typical neuron with class 2 response (monophasic excitatory response). **D.** Z-scored PSTH of all responsive SNr neurons clustered by K-means clustering (top) and the mean PSTH of each cluster (bottom). Colors correspond to cluster numbers. The thickness indicates the numbers of neurons in the cluster. **E,F.** Examples of SNr neurons that were classified as class 1 but also received class-2-like monophasic excitatory input. **G,H,I**. Neurons showing a very fast excitatory monophasic response (**G**), monophasic inhibitory response (**H**), and inhibition-excitation pattern (**I**). **J.** Average input maps of neurons with class 1 (left) and class 2 (right) responses in SNr. **K.** An inhibitory response map of cluster #1 neurons in SNr. **L.** Time courses of the responsive areas. **M.** The same analysis as **D**, but separated according to recording location. Black and gray circles indicate triphasic and inhibition-excitation patterns, respectively. **Extended Data 2** is available for additional analysis on the SNr data.

Extended Data 2. Hyperdirect, direct, and indirect pathways are explained by basal ganglia, not by synaptic interaction within the SNr. **A.** An example of cross-correlogram showing inhibitory interaction between simultaneously recorded pair of SNr neurons. The synaptic interaction does not explain the PSTHs. The PSTHs were obtained with the responsive pixels that shared by the two neurons. **B,C.** Examples of the other SNr neuron pairs. **D.** Schematic of the hyperdirect, direct, and indirect pathways.

Figure 5. A retrograde tracer revealing thalamic projections from substantia nigra pars reticulata (SNr) and cerebellar nuclei (CN).

A. Schematic of tracer experiments. **B.** Sagittal section 2 weeks after injection of AAVretro-CAG-tdTomato into the VL nucleus of thalamus. White is DAPI fluorescence showing localization of DNA. **C.** The tdTomato fluorescence around the ipsilateral SNr. **D.** Expanded image corresponding to the rectangle in **C. E.** The tdTomato fluorescence around the contralateral CN (LCN, lateral cerebellar nucleus). **F.** Expanded image corresponding to the rectangle in **E. G.** Axon collateral of CN neurons into the cerebral granule cell layer. **H.** Expanded image corresponding to the rectangle in **G. I.** The tdTomato fluorescence around the ipsilateral motor cortex. **J.** Expanded image corresponding to the rectangle in top panel. **K-O.** The same images as **B-F** of an injection experiment to the VM nucleus of thalamus. **P-T.** The same images as **B-F** of an injection experiment to the VA nucleus of thalamus.

Figure 6. Activity propagation from the cerebellum to the striatum.

A. Approximate positions of recording pass 1 for CN, pass 2 for the thalamus, and pass 3 for the motor cortex and striatum. The mirror was positioned behind the cerebellum to direct the laser to CN. **B.** A headplate optimized for this experiment. **C.** The cerebellum viewed from the angle of laser incidence. The blue frame indicates the photostimulation area. The approximate position of the lateral (purple), interposed (orange), and medial (green) nucleus were overlayed. **D.** Representative fluorescence image used to identify the location of the recording electrode. **E.** A photograph during photostimulation of the cerebellum and recording at the contralateral cerebral cortex. **F.** A photograph of transparent skull on the cerebellum (top). A response map was overlayed (bottom). **G.** Response map (left) and map of the peak latency (right) of a neuron recorded in interposed CN. **H.** The PSTHs of the receptive fields. **I.** Latency histograms of all neurons recorded in CNs. **J-L.** The same analysis as **G-I** for neurons in VL. **M-O.** The same analysis as **G-I** for neurons in CL. **P-R.** The same analysis as **G-I** for neurons in motor cortex. **S-U.** The same analysis as **G-I** for neurons in striatum.

Figure 7. Simulation of spiking neurons based on the connectome data.

A. Circuit schematic of the basal ganglia and cerebellum. In the basal ganglia, submodule-level details were constructed based on connectome data. Both share input from the cerebral cortex and output to the thalamus. **B.** Raster plot of simulated neurons before and after stimulation (single trial). **C.** PSTHs of major neurons in the basal ganglia under control conditions and after blocking the hyperdirect, direct, and indirect pathways. Colors indicate submodules. **D.** PSTHs of major neurons in the cerebellum under control conditions and after blocking MF-CN

synapses (P1) and PC-CN synapses (P2). **E.** Simplified circuit for the simulation of VM and VL (top). Raster plots and PSTHs of VM and VL neurons (bottom). **F.** L5PN was assumed to receive both inputs from VM and VL (top left). The firing rate of L5PN was simulated when the signal from cerebellum was delayed (left), or when the signal from basal ganglia was delayed (right). **G.** Maximum firing rate of the L5PN at the fast peak (<50 ms) as a function of the delay-time of basal ganglia (purple) and cerebellum (green) (top). The same analysis for the late peak (>50 ms) (bottom)**. Extended Data 3** is available for additional data and analysis.

Extended Data 3. The network of cerebral cortex, cerebellum, and basal ganglia.
A. A circuit diagram with parameters (w: weight in mV, p: probability, and delay in ms)**. B.** Based on anatomical data, we constructed a detailed circuit consisting of 16 modules of striatum, 36 modules of external globus pallidus, 3 modules of subthalamic nucleus, and 14 modules of substantia nigra pars reticulata. Each line indicates a connection between subdivisions. The three rectangular frames indicate known clusters (Foster et al. 2021). Connections among CP (or ACB) (caudate putamen or nucleus accumbens, total 16 clusters), GPe (36 clusters), STN (3 clusters), SNr (14 clusters) were determined according to (Foster et al. 2021, Jeon et al. 2022, Hintiryan et al. 2016). Line colors indicate connection types.

Figure 8. Reservoir-reinforced learning model of the cortex, cerebellum, and basal ganglia.

A. The task structure. The agent is rewarded for holding the lever for 1 s followed by a sound cue and pulling the lever within 0.3 s. **B.** Double-exponential curves mimicking substantia nigra pars reticulata (SNr) (left) and cerebellar nuclei (CN) (right) activity. **C.** Schematic of the model. Cerebral cortex activity was simulated by a reservoir circuit that receives sound and reward inputs. The basal ganglia and cerebellum each integrate three synaptic strengths and three functions, each of which mimic the experimental data. The output from basal ganglia and cerebellum finally combined to a pull value and hold value. The difference between these values determined pull or hold once in 100 ms. Synaptic plasticity was induced by RPE. **D.** Examples of 6 s time series, pull or hold values, movement outputs, sound cues, and rewards in early to late learning stages. **E.** Learning curves under control conditions and after blocking synaptic plasticity in basal ganglia or cerebellum (left). The reward number in the late learning period after 50% blocking each pathway (right). HD; hyper direct, D; direct, ID; indirect, P1; phase 1 , P2; phase2, P3; phase 3. **F.** Time course of direct pathway output (green) and P1 pathway output (purple) at 200 ms after tone presentation during learning. **G.** The same analysis as in f, but 600 ms after tone presentation. **H.** Schematic of signal delay(left). Changes in learning curves after delaying the conduction of corticostriatal or corticopontine projections. A 10 ms delay slowed the learning rate. **I.** Example of the activity of 50 units when the time constant tau of each unit in the reservoir was changed from 5 to 50 ms. **J.** Timescale of cortical neural activity indicated by colors affects the conduction-delay dependency of learning. **K**. Gain in learning rate when delay time was zero based on delay time plus or minus 70 ms. **Extended Data 4** is available for additional data and analysis.

Extended Data 4. Noise and oscillatory input dependences of reinforcement learning.
A. An illustration of independent noise input to the basal ganglia and cerebellum, or oscillatory input to the cerebral cortex (reservoir). **B**. Example of 100 neural activities of the reservoir circuit. Left, original neural activity. Right, neural activity when noise was added at twice the standard deviation of the neural activity. **C.** Number of reward acquisitions (10 s) during early and late learning periods when independent noise was applied to inputs to the basal ganglia and cerebellum. Learning efficiency did not deteriorate until the noise was about twice the standard deviation of the neural activity. **D**. Example of 100 neural activities of the reservoir circuit. **E.** Dependence of the number of reward acquisitions (10 sec) in the early and late learning periods on the amplitude of the beta oscillation. **F.** Power spectral density as a function of the frequency of the sine wave. **G.** Power spectral density of the number of reward acquisitions (10 sec) in the early and late learning periods. **H.** Time-delay dependence of the number of reward acquisitions (10 s) in the early and late learning periods with beta oscillations (20 Hz). A periodicity of about 50 ms, i.e., 20 Hz, was observed. This indicates that the phase difference between the basal ganglia and the cerebellum is involved in learning. **I.** ×0.8 (shorter, pink) or ×1.5 (longer, orange) time scale for CN and SNr response functions (**left**). Power spectrum density of the sum of CN and SNr responses (**middle**). Using original (blue), shorter (pink) or longer (orange) time scale filter, the number of rewards in the late learning period at each of the 10-30 Hz cortical oscillation frequencies was plotted against the cortical oscillation frequency (**right**). **J.** The power spectrum of the sum of all response functions when either the basal ganglia or cerebellar response function was delayed was plotted against the time delay of the basal ganglia or cerebellar response function. **K.** Parallel linear system consisting of the cortex (X), basal ganglia (B), and cerebellum (C). See main text for details. **L, M, and N.** The same analysis as in

Figure 8E, H and **Extended Data 4G**, respectively, was performed by changing the time step for action from 100 ms to 50 ms. All showed qualitatively similar results.

Table 1. A lens data list of the scanning optogenetics system. Shaded areas highlight substitutes of the Nikon camera lens with f = 105 mm.

Table 2. The numbers of neurons, numbers of domains, spontaneous firing rate, and four parameters of the Izhikevich model. FSI: fast spiking interneuron, MSN: medium spiny neuron, GPe: external segment of global pallidus, STN: subthalamic nucleus, SNr: substantia nigra pars reticulata, GPi: internal segment of global pallidus, ST: stellate cell, BA: basket cell, GO: Golgi cell, GR: granule cell, PC: Purkinje cell, IO: inferior olive cell, MF: mossy fiber, DCN: deep cerebellar nucleus, VM: ventromedial nucleus, VL: ventrolateral nucleus. L5PN; layer 5 pyramidal neuron. The number of neurons in each type in basal ganglia, cerebellum, and PF were determined by the single-cell-resolution whole-brain atlas (Murakami et al. 2018).

Supplementary information

The code of the spiking neural network, code of reservoir model, CAD files of the headplate, parts list, Zemax files for the scan-optogenetics system will be made available upon publication. Electrophysiological data is available upon request.

References

Aizenman, Carlos D, and David J Linden. 1999. 'Regulation of the rebound depolarization and spontaneous firing patterns of deep nuclear neurons in slices of rat cerebellum', *Journal of neurophysiology*, 82: 1697-709.

Alexander, Garrett E, and Michael D Crutcher. 1990. 'Functional architecture of basal ganglia circuits: neural substrates of parallel processing', *Trends in neurosciences*, 13: 266-71.

Alexander, Garrett E, Mahlon R DeLong, and Peter L Strick. 1986. 'Parallel organization of functionally segregated circuits linking basal ganglia and cortex', *Annual review of neuroscience*, 9: 357-81.

Allen, GI, and N Tsukahara. 1974. 'Cerebrocerebellar communication systems', *Physiological reviews*, 54: 957-1006.

Barthas, Florent, and Alex C Kwan. 2017. 'Secondary motor cortex: where 'sensory' meets 'motor' in the rodent frontal cortex', *Trends in neurosciences*, 40: 181-93.

Beau, Maxime, David J Herzfeld, Francisco Naveros, Marie E Hemelt, Federico D' Agostino, Marlies Oostland, Alvaro Sánchez-López, Young Yoon Chung, Michael Maibach, and Stephen Kyranakis. 2024. 'A deep-learning strategy to identify cell types across species from high-density extracellular recordings', *bioRxiv*: 2024.01. 30.577845.

Berke, Joshua D, Murat Okatan, Jennifer Skurski, and Howard B Eichenbaum. 2004. 'Oscillatory entrainment of striatal neurons in freely moving rats', *Neuron*, 43: 883-96.

Bostan, Andreea C, and Peter L Strick. 2018. 'The basal ganglia and the cerebellum: nodes in an integrated network', *Nature Reviews Neuroscience*, 19: 338-50.

Boven, Ellen, Joseph Pemberton, Paul Chadderton, Richard Apps, and Rui Ponte Costa. 2023. 'Cerebro-cerebellar networks facilitate learning through feedback decoupling', *Nature communications*, 14: 51.

Caligiore, Daniele, Michael A Arbib, R Chris Miall, and Gianluca Baldassarre. 2019. 'The super-learning hypothesis: Integrating learning processes across cortex, cerebellum and basal ganglia', *Neuroscience & Biobehavioral Reviews*, 100: 19-34.

Caligiore, Daniele, Giovanni Pezzulo, Gianluca Baldassarre, Andreea C Bostan, Peter L Strick, Kenji Doya, Rick C Helmich, Michiel Dirkx, James Houk, and Henrik Jörntell. 2017. 'Consensus paper: towards a systems-level view of cerebellar function: the interplay between cerebellum, basal ganglia, and cortex', *The Cerebellum*, 16: 203-29.

Chabrol, Francois P, Antonin Blot, and Thomas D Mrsic-Flogel. 2019. 'Cerebellar contribution to preparatory activity in motor neocortex', *Neuron*, 103: 506-19.

e4.
Chantranupong, Lynne, Celia C Beron, Joshua A Zimmer, Michelle J Wen, Wengang Wang, and Bernardo L Sabatini. 2023. 'Dopamine and glutamate regulate striatal acetylcholine in decision-making', *Nature*, 621: 577-85.
Chen, Christopher H, Rachel Fremont, Eduardo E Arteaga-Bracho, and Kamran Khodakhah. 2014. 'Short latency cerebellar modulation of the basal ganglia', *Nature neuroscience*, 17: 1767-75.
Chen, Guozhang, Franz Scherr, and Wolfgang Maass. 2022. 'A data-based large-scale model for primary visual cortex enables brain-like robust and versatile visual processing', *science advances*, 8: eabq7592.
Cheron, Guy, Matthias Sausbier, Ulrike Sausbier, Winfried Neuhuber, Peter Ruth, Bernard Dan, and Laurent Servais. 2009. 'BK channels control cerebellar Purkinje and Golgi cell rhythmicity in vivo', *PloS one*, 4: e7991.
Chiken, Satomi, Pullanipally Shashidharan, and Atsushi Nambu. 2008. 'Cortically evoked long-lasting inhibition of pallidal neurons in a transgenic mouse model of dystonia', *Journal of Neuroscience*, 28: 13967-77.
Courtemanche, Richard, Jennifer C Robinson, and Daniel I Aponte. 2013. 'Linking oscillations in cerebellar circuits', *Frontiers in Neural Circuits*
7: 125.
Diedrichsen, Jörn, Richard B Ivry, and Jeff Pressing. 2003. 'Cerebellar and basal ganglia contributions to interval timing', *Functional and neural mechanisms of interval timing*: 457-81.
Doya, Kenji. 1999. 'What are the computations of the cerebellum, the basal ganglia and the cerebral cortex?', *Neural networks*, 12: 961-74.
——. 2000. 'Complementary roles of basal ganglia and cerebellum in learning and motor control', *Current Opinion in Neurobiology*, 10: 732-39.
Foster, Nicholas N, Joshua Barry, Laura Korobkova, Luis Garcia, Lei Gao, Marlene Becerra, Yasmine Sherafat, Bo Peng, Xiangning Li, and Jun-Hyeok Choi. 2021. 'The mouse cortico-basal ganglia-thalamic network', *Nature*, 598: 188-94.
Fujimoto, K, and H Kita. 1992. 'Responses of rat substantia nigra pars reticulata units to cortical stimulation', *Neuroscience letters*, 142: 105-09.
Gage, Gregory J, Colin R Stoetzner, Alexander B Wiltschko, and Joshua D Berke. 2010. 'Selective activation of striatal fast-spiking interneurons during choice execution', *Neuron*, 67: 466-79.
Gambosi, Benedetta, Francesco Jamal Sheiban, Marco Biasizzo, Alberto Antonietti, Egidio D'angelo, Alberto Mazzoni, and Alessandra Pedrocchi. 2024. 'A model with dopamine

depletion in basal ganglia and cerebellum predicts changes in thalamocortical beta oscillations', *International Journal of Neural Systems*, 2450045: 21.

Gao, Zhenyu, Courtney Davis, Alyse M Thomas, Michael N Economo, Amada M Abrego, Karel Svoboda, Chris I De Zeeuw, and Nuo Li. 2018. 'A cortico-cerebellar loop for motor planning', *Nature*, 563: 113-16.

Gornati, Simona V, Carmen B Schäfer, Oscar HJ Eelkman Rooda, Alex L Nigg, Chris I De Zeeuw, and Freek E Hoebeek. 2018. 'Differentiating cerebellar impact on thalamic nuclei', *Cell reports*, 23: 2690-704.

Grillner, Sten. 2021. 'Evolution of the vertebrate motor system—from forebrain to spinal cord', *Current Opinion in Neurobiology*, 71: 11-18.

Halje, Pär, Ivani Brys, Juan J Mariman, Claudio Da Cunha, Romulo Fuentes, and Per Petersson. 2019. 'Oscillations in cortico-basal ganglia circuits: implications for Parkinson's disease and other neurologic and psychiatric conditions', *Journal of neurophysiology*, 122: 203-31.

Harvey, RJ, R Porter, and JA Rawson. 1979. 'Discharges of intracerebellar nuclear cells in monkeys', *The Journal of physiology*, 297: 559-80.

Heffley, William, and Court Hull. 2019. 'Classical conditioning drives learned reward prediction signals in climbing fibers across the lateral cerebellum', *Elife*, 8: e46764.

Hesslow, Germund, Pär Svensson, and Magnus Ivarsson. 1999. 'Learned movements elicited by direct stimulation of cerebellar mossy fiber afferents', *Neuron*, 24: 179-85.

Hintiryan, Houri, Nicholas N Foster, Ian Bowman, Maxwell Bay, Monica Y Song, Lin Gou, Seita Yamashita, Michael S Bienkowski, Brian Zingg, and Muye Zhu. 2016. 'The mouse cortico-striatal projectome', *Nature neuroscience*, 19: 1100-14.

Hira, Riichiro, Naoki Honkura, Jun Noguchi, Yoshio Maruyama, George J Augustine, Haruo Kasai, and Masanori Matsuzaki. 2009. 'Transcranial optogenetic stimulation for functional mapping of the motor cortex', *Journal of neuroscience methods*, 179: 258-63.

Hira, Riichiro, Fuki Ohkubo, Katsuya Ozawa, Yoshikazu Isomura, Kazuo Kitamura, Masanobu Kano, Haruo Kasai, and Masanori Matsuzaki. 2013. 'Spatiotemporal dynamics of functional clusters of neurons in the mouse motor cortex during a voluntary movement', *Journal of Neuroscience*, 33: 1377-90.

Hira, Riichiro, Fuki Ohkubo, Yasuhiro R Tanaka, Yoshito Masamizu, George J Augustine, Haruo Kasai, and Masanori Matsuzaki. 2013. 'In vivo optogenetic tracing of functional corticocortical connections between motor forelimb areas', *Frontiers in Neural Circuits*

7: 55.

Hira, Riichiro, Shin-Ichiro Terada, Masashi Kondo, and Masanori Matsuzaki. 2015. 'Distinct functional modules for discrete and rhythmic forelimb movements in the mouse motor cortex', *Journal of Neuroscience*, 35: 13311-22.

Hira, Riichiro, Leah B Townsend, Ikuko T Smith, Che-Hang Yu, Jeffrey N Stirman, Yiyi Yu, and Spencer LaVere Smith. 2023. 'Mesoscale functional architecture in medial posterior parietal cortex', *bioRxiv*: 2023.08. 27.555017.

Hirano, T. 1990. 'Depression and potentiation of the synaptic transmission between a granule cell and a Purkinje cell in rat cerebellar culture', *Neuroscience letters*, 119: 141-44.

Hoang, Huu, Shinichiro Tsutsumi, Masanori Matsuzaki, Masanobu Kano, Mitsuo Kawato, Kazuo Kitamura, and Keisuke Toyama. 2023. 'Dynamic organization of cerebellar climbing fiber response and synchrony in multiple functional components reduces dimensions for reinforcement learning', *Elife*, 12: e86340.

Hoebeek, Freek E, Laurens Witter, Tom JH Ruigrok, and Chris I De Zeeuw. 2010. 'Differential olivo-cerebellar cortical control of rebound activity in the cerebellar nuclei', *Proceedings of the National Academy of Sciences*, 107: 8410-15.

Hooks, Bryan M, Tianyi Mao, Diego A Gutnisky, Naoki Yamawaki, Karel Svoboda, and Gordon MG Shepherd. 2013. 'Organization of cortical and thalamic input to pyramidal neurons in mouse motor cortex', *Journal of Neuroscience*, 33: 748-60.

Houk, James C, C Bastianen, D Fansler, A Fishbach, D Fraser, PJ Reber, SA Roy, and LS Simo. 2007. 'Action selection and refinement in subcortical loops through basal ganglia and cerebellum', *Philosophical Transactions of the Royal Society B: Biological Sciences*, 362: 1573-83.

Houk, James C, and Steven P Wise. 1995. 'Distributed modular architectures linking basal ganglia, cerebellum, and cerebral cortex: their role in planning and controlling action', *Cerebral cortex*, 5: 95-110.

Ichinohe, Noritaka, Fumiaki Mori, and Kazuhiko Shoumura. 2000. 'A di-synaptic projection from the lateral cerebellar nucleus to the laterodorsal part of the striatum via the central lateral nucleus of the thalamus in the rat', *Brain Research*, 880: 191-97.

Igarashi, Jun, Yoshikazu Isomura, Kensuke Arai, Rie Harukuni, and Tomoki Fukai. 2013. 'A $\theta-\gamma$ oscillation code for neuronal coordination during motor behavior', *Journal of Neuroscience*, 33: 18515-30.

Izhikevich, Eugene M. 2003. 'Simple model of spiking neurons', *IEEE Transactions on neural networks*, 14: 1569-72.

——. 2007. *Dynamical systems in neuroscience* (MIT press).

Jelitai, Marta, Paolo Puggioni, Taro Ishikawa, Arianna Rinaldi, and Ian Duguid. 2016. 'Dendritic excitation-inhibition balance shapes cerebellar output during motor behaviour', *Nature communications*, 7: 13722.

Jeon, Hyungju, Hojin Lee, Dae-Hyuk Kwon, Jiwon Kim, Keiko Tanaka-Yamamoto, Jang Soo Yook, Linqing Feng, Hye Ran Park, Yong Hoon Lim, and Zang-Hee Cho. 2022. 'Topographic connectivity and cellular profiling reveal detailed input pathways and functionally distinct cell types in the subthalamic nucleus', *Cell reports*, 38.

Jun, James J, Nicholas A Steinmetz, Joshua H Siegle, Daniel J Denman, Marius Bauza, Brian Barbarits, Albert K Lee, Costas A Anastassiou, Alexandru Andrei, and Çağatay Aydın. 2017. 'Fully integrated silicon probes for high-density recording of neural activity', *Nature*, 551: 232-36.

Kaneko, Takeshi. 2013. 'Local connections of excitatory neurons in motor-associated cortical areas of the rat', *Frontiers in Neural Circuits*
7: 75.

Kawabata, Masanori, Shogo Soma, Akiko Saiki-Ishikawa, Satoshi Nonomura, Junichi Yoshida, Alain Ríos, Yutaka Sakai, and Yoshikazu Isomura. 2020. 'A spike analysis method for characterizing neurons based on phase locking and scaling to the interval between two behavioral events', *Journal of neurophysiology*, 124: 1923-41.

Kebschull, Justus M, Ethan B Richman, Noam Ringach, Drew Friedmann, Eddy Albarran, Sai Saroja Kolluru, Robert C Jones, William E Allen, Ying Wang, and Seung Woo Cho. 2020. 'Cerebellar nuclei evolved by repeatedly duplicating a conserved cell-type set', *Science*, 370: eabd5059.

Khanna, Preeya, and Jose M Carmena. 2015. 'Neural oscillations: beta band activity across motor networks', *Current Opinion in Neurobiology*, 32: 60-67.

Kimura, Rie, Akiko Saiki, Yoko Fujiwara-Tsukamoto, Fuki Ohkubo, Kazuo Kitamura, Masanori Matsuzaki, Yutaka Sakai, and Yoshikazu Isomura. 2012. 'Reinforcing operandum: rapid and reliable learning of skilled forelimb movements by head-fixed rodents', *Journal of neurophysiology*, 108: 1781-92.

Kimura, Rie, Akiko Saiki, Yoko Fujiwara‐Tsukamoto, Yutaka Sakai, and Yoshikazu Isomura. 2017. 'Large‐scale analysis reveals populational contributions of cortical spike rate and synchrony to behavioural functions', *The Journal of physiology*, 595: 385-413.

Kitano, Hiroyuki, Ikuo Tanibuchi, and Kohnosuke Jinnai. 1998. 'The distribution of neurons in the substantia nigra pars reticulata with input from the motor, premotor and prefrontal areas of the cerebral cortex in monkeys', *Brain Research*, 784: 228-38.

Kostadinov, Dimitar, and Michael Häusser. 2022. 'Reward signals in the cerebellum: origins, targets, and functional implications', *Neuron*.

Kuramoto, Eriko, Takahiro Furuta, Kouichi C Nakamura, Tomo Unzai, Hiroyuki Hioki, and Takeshi Kaneko. 2009. 'Two types of thalamocortical projections from the motor thalamic nuclei of the rat: a single neuron-tracing study using viral vectors', *Cerebral cortex*, 19: 2065-77.

Kuramoto, Eriko, Sachi Ohno, Takahiro Furuta, Tomo Unzai, Yasuhiro R Tanaka, Hiroyuki Hioki, and Takeshi Kaneko. 2015. 'Ventral medial nucleus neurons send thalamocortical afferents more widely and more preferentially to layer 1 than neurons of the ventral anterior-ventral lateral nuclear complex in the rat', *Cerebral cortex*, 25: 221-35.

Lacefield, Clay O, Eftychios A Pnevmatikakis, Liam Paninski, and Randy M Bruno. 2019. 'Reinforcement learning recruits somata and apical dendrites across layers of primary sensory cortex', *Cell reports*, 26: 2000-08. e2.

Lake, Brenden M, Tomer D Ullman, Joshua B Tenenbaum, and Samuel J Gershman. 2017. 'Building machines that learn and think like people', *Behavioral and brain sciences*, 40: e253.

Ledergerber, Debora, and Matthew Evan Larkum. 2012. 'The time window for generation of dendritic spikes by coincidence of action potentials and EPSPs is layer specific in somatosensory cortex', *PloS one*, 7: e33146.

Lee, Dongmin, Jung Ho Hyun, Kanghoon Jung, Patrick Hannan, and Hyung-Bae Kwon. 2017. 'A calcium-and light-gated switch to induce gene expression in activated neurons', *Nature biotechnology*, 35: 858-63.

Lee, Jaeeon, Wengang Wang, and Bernardo L Sabatini. 2020. 'Anatomically segregated basal ganglia pathways allow parallel behavioral modulation', *Nature neuroscience*, 23: 1388-98.

Leventhal, Daniel K, Gregory J Gage, Robert Schmidt, Jeffrey R Pettibone, Alaina C Case, and Joshua D Berke. 2012. 'Basal ganglia beta oscillations accompany cue utilization', *Neuron*, 73: 523-36.

Li, Tianbai, Weidong Le, and Joseph Jankovic. 2023. 'Linking the cerebellum to Parkinson disease: an update', *Nature Reviews Neurology*, 19: 645-54.

Mallet, Nicolas, Alek Pogosyan, László F Márton, J Paul Bolam, Peter Brown, and Peter J Magill. 2008. 'Parkinsonian beta oscillations in the external globus pallidus and their relationship with subthalamic nucleus activity', *Journal of Neuroscience*, 28: 14245-58.

Marlinski, Vladimir, and Irina N Beloozerova. 2014. 'Burst firing of neurons in the thalamic reticular nucleus during locomotion', *Journal of neurophysiology*, 112:

181-92.

Maurice, Nicolas, Jean-Michel Deniau, Jacques Glowinski, and Anne-Marie Thierry. 1999. 'Relationships between the prefrontal cortex and the basal ganglia in the rat: physiology of the cortico-nigral circuits', *Journal of Neuroscience*, 19: 4674-81.

Maurice, Nicolas, Anne-Marie Thierry, Jacques Glowinski, and Jean-Michel Deniau. 2003. 'Spontaneous and evoked activity of substantia nigra pars reticulata neurons during high-frequency stimulation of the subthalamic nucleus', *Journal of Neuroscience*, 23: 9929-36.

Middleton, Steven J, Claudia Racca, Mark O Cunningham, Roger D Traub, Hannah Monyer, Thomas Knöpfel, Ian S Schofield, Alistair Jenkins, and Miles A Whittington. 2008. 'High-frequency network oscillations in cerebellar cortex', *Neuron*, 58: 763-74.

Miller, Benjamin R, Adam G Walker, Anand S Shah, Scott J Barton, and George V Rebec. 2008. 'Dysregulated information processing by medium spiny neurons in striatum of freely behaving mouse models of Huntington's disease', *Journal of neurophysiology*, 100: 2205-16.

Mitani, Keita, Masanori Kawabata, Yoshikazu Isomura, and Yutaka Sakai. 2022. 'Automated and parallelized spike collision tests to identify spike signal projections', *Iscience*, 25.

Morén, Jan, Jun Igarashi, Osamu Shouno, Junichiro Yoshimoto, and Kenji Doya. 2019. 'Dynamics of basal ganglia and thalamus in Parkinsonian tremor', *Multiscale Models of Brain Disorders*: 13-20.

Muddapu, Vignayanandam Ravindernath, Alekhya Mandali, V Srinivasa Chakravarthy, and Srikanth Ramaswamy. 2019. 'A computational model of loss of dopaminergic cells in Parkinson's disease due to glutamate-induced excitotoxicity', *Frontiers in Neural Circuits*
13: 11.

Murakami, Tatsuya C, Tomoyuki Mano, Shu Saikawa, Shuhei A Horiguchi, Daichi Shigeta, Kousuke Baba, Hiroshi Sekiya, Yoshihiro Shimizu, Kenji F Tanaka, and Hiroshi Kiyonari. 2018. 'A three-dimensional single-cell-resolution whole-brain atlas using CUBIC-X expansion microscopy and tissue clearing', *Nature neuroscience*, 21: 625-37.

Mushiake, HAJIME, and PETER L Strick. 1993. 'Preferential activity of dentate neurons during limb movements guided by vision', *Journal of neurophysiology*, 70: 2660-64.

Muzzu, Tomaso, Susanna Mitolo, Giuseppe P Gava, and Simon R Schultz. 2018. 'Encoding of locomotion kinematics in the mouse cerebellum', *PloS one*, 13: e0203900.

Nambu, Atsushi, Satomi Chiken, Hiromi Sano, Nobuhiko Hatanaka, and José A Obeso. 2023.

'Dynamic Activity Model of Movement Disorders: The Fundamental Role of the Hyperdirect Pathway', *Movement Disorders*, 38: 2145-50.

Nambu, Atsushi, Hironobu Tokuno, Ikuma Hamada, Hitoshi Kita, Michiko Imanishi, Toshikazu Akazawa, Yoko Ikeuchi, and Naomi Hasegawa. 2000. 'Excitatory cortical inputs to pallidal neurons via the subthalamic nucleus in the monkey', *Journal of neurophysiology*, 84: 289-300.

Nambu, Atsushi, Hironobu Tokuno, and Masahiko Takada. 2002. 'Functional significance of the cortico-subthalamo-pallidal 'hyperdirect' pathway', *Neuroscience Research*, 43: 111-17.

O'Connor, Daniel H, Simon P Peron, Daniel Huber, and Karel Svoboda. 2010. 'Neural activity in barrel cortex underlying vibrissa-based object localization in mice', *Neuron*, 67: 1048-61.

Ohmae, Shogo, Jun Kunimatsu, and Masaki Tanaka. 2017. 'Cerebellar roles in self-timing for sub-and supra-second intervals', *Journal of Neuroscience*, 37: 3511-22.

Pemberton, Joseph, Paul Chadderton, and Rui Ponte Costa. 2022. 'Cerebellar-driven cortical dynamics enable task acquisition, switching and consolidation', *bioRxiv*: 2022.11.14.516257.

Penhune, Virginia B, and Christopher J Steele. 2012. 'Parallel contributions of cerebellar, striatal and M1 mechanisms to motor sequence learning', *Behavioural brain research*, 226: 579-91.

Petter, Elijah A, Nicholas A Lusk, Germund Hesslow, and Warren H Meck. 2016. 'Interactive roles of the cerebellum and striatum in sub-second and supra-second timing: Support for an initiation, continuation, adjustment, and termination (ICAT) model of temporal processing', *Neuroscience & Biobehavioral Reviews*, 71: 739-55.

Pisano, Thomas J, Zahra M Dhanerawala, Mikhail Kislin, Dariya Bakshinskaya, Esteban A Engel, Ethan J Hansen, Austin T Hoag, Junuk Lee, Nina L de Oude, and Kannan Umadevi Venkataraju. 2021. 'Homologous organization of cerebellar pathways to sensory, motor, and associative forebrain', *Cell reports*, 36: 109721.

Poirazi, Panayiota, and Athanasia Papoutsi. 2020. 'Illuminating dendritic function with computational models', *Nature Reviews Neuroscience*, 21: 303-21.

Popa, Daniela, Maria Spolidoro, Rémi D Proville, Nicolas Guyon, Lucile Belliveau, and Clément Léna. 2013. 'Functional role of the cerebellum in gamma-band synchronization of the sensory and motor cortices', *Journal of Neuroscience*, 33: 6552-56.

Popa, T, B Velayudhan, C Hubsch, S Pradeep, E Roze, M Vidailhet, S Meunier, and A Kishore. 2013. 'Cerebellar processing of sensory inputs primes motor cortex plasticity',

1485 *Cerebral cortex*, 23: 305-14.
1486 Proville, Rémi D, Maria Spolidoro, Nicolas Guyon, Guillaume P Dugué, Fekrije Selimi,
1487 Philippe Isope, Daniela Popa, and Clément Léna. 2014. 'Cerebellum involvement in
1488 cortical sensorimotor circuits for the control of voluntary movements', *Nature*
1489 *neuroscience*, 17: 1233-39.
1490 Prsa, Mario, Suryadeep Dash, Nicolas Catz, Peter W Dicke, and Peter Thier. 2009.
1491 'Characteristics of responses of Golgi cells and mossy fibers to eye saccades and
1492 saccadic adaptation recorded from the posterior vermis of the cerebellum', *Journal*
1493 *of Neuroscience*, 29: 250-62.
1494 Pugh, Jason R, and Indira M Raman. 2008. 'Mechanisms of potentiation of mossy fiber EPSCs
1495 in the cerebellar nuclei by coincident synaptic excitation and inhibition',
1496 *Journal of Neuroscience*, 28: 10549-60.
1497 Saiki, Akiko, Yutaka Sakai, Ryoji Fukabori, Shogo Soma, Junichi Yoshida, Masanori Kawabata,
1498 Hiromu Yawo, Kazuto Kobayashi, Minoru Kimura, and Yoshikazu Isomura. 2018. 'In
1499 vivo spiking dynamics of intra-and extratelencephalic projection neurons in rat
1500 motor cortex', *Cerebral cortex*, 28: 1024-38.
1501 Sano, Hiromi, Satomi Chiken, Takatoshi Hikida, Kazuto Kobayashi, and Atsushi Nambu. 2013.
1502 'Signals through the striatopallidal indirect pathway stop movements by phasic
1503 excitation in the substantia nigra', *Journal of Neuroscience*, 33: 7583-94.
1504 Schell, GERALD R, and PETER L Strick. 1984. 'The origin of thalamic inputs to the arcuate
1505 premotor and supplementary motor areas', *Journal of Neuroscience*, 4: 539-60.
1506 Sedaghat-Nejad, Ehsan, Mohammad Amin Fakharian, Jay Pi, Paul Hage, Yoshiko Kojima, Robi
1507 Soetedjo, Shogo Ohmae, Javier F Medina, and Reza Shadmehr. 2021. 'P-sort: an
1508 open-source software for cerebellar neurophysiology', *Journal of neurophysiology*,
1509 126: 1055-75.
1510 Sedaghat-Nejad, Ehsan, Jay S Pi, Paul Hage, Mohammad Amin Fakharian, and Reza Shadmehr.
1511 2022. 'Synchronous spiking of cerebellar Purkinje cells during control of
1512 movements', *Proceedings of the National Academy of Sciences*, 119: e2118954119.
1513 Sendhilnathan, Naveen, Mulugeta Semework, Michael E Goldberg, and Anna E Ipata. 2020.
1514 'Neural correlates of reinforcement learning in mid-lateral cerebellum', *Neuron*,
1515 106: 188-98. e5.
1516 Shadmehr, Reza, and John W Krakauer. 2008. 'A computational neuroanatomy for motor control',
1517 *Experimental brain research*, 185: 359-81.
1518 Shen, Weixing, Joshua L Plotkin, Veronica Francardo, Wai Kin D Ko, Zhong Xie, Qin Li, Tim
1519 Fieblinger, Jürgen Wess, Richard R Neubig, and Craig W Lindsley. 2015. 'M4
1520 muscarinic receptor signaling ameliorates striatal plasticity deficits in models

of L-DOPA-induced dyskinesia', *Neuron*, 88: 762-73.

Shinoda, Y, Y Sugiuchi, T Futami, and R Izawa. 1992. 'Axon collaterals of mossy fibers from the pontine nucleus in the cerebellar dentate nucleus', *Journal of neurophysiology*, 67: 547-60.

Siegle, Joshua H, Aarón Cuevas López, Yogi A Patel, Kirill Abramov, Shay Ohayon, and Jakob Voigts. 2017. 'Open Ephys: an open-source, plugin-based platform for multichannel electrophysiology', *Journal of neural engineering*, 14: 045003.

Spencer, Rebecca MC, and Richard B Ivry. 2021. 'Cerebellum and timing.' in, *Handbook of the cerebellum and cerebellar disorders* (Springer).

Stein, Edward, and Izhar Bar-Gad. 2013. 'Beta oscillations in the cortico-basal ganglia loop during parkinsonism', *Experimental Neurology*, 245: 52-59.

Sugihara, I, H Wu, and Y Shinoda. 1996. 'Morphology of axon collaterals of single climbing fibers in the deep cerebellar nuclei of the rat', *Neuroscience letters*, 217: 33-36.

Sugihara, Izumi, Hirofumi Fujita, Jie Na, Pham Nguyen Quy, Bing-Yang Li, and Daisuke Ikeda. 2009. 'Projection of reconstructed single Purkinje cell axons in relation to the cortical and nuclear aldolase C compartments of the rat cerebellum', *Journal of Comparative Neurology*, 512: 282-304.

Sugino, Hikaru, Sho Tanno, Tatsumi Yoshida, Yoshikazu Isomura, and Riichiro Hira. 2024. 'Functional segregation and dynamic integration of the corticotectal descending signal in rat', *Neuroscience Research*.

Tanaka, Masaki, Masashi Kameda, and Ken-ichi Okada. 2024. 'Temporal Information Processing in the Cerebellum and Basal Ganglia', *Neurobiology of Interval Timing*: 95-116.

Tervo, D Gowanlock R, Bum-Yeol Hwang, Sarada Viswanathan, Thomas Gaj, Maria Lavzin, Kimberly D Ritola, Sarah Lindo, Susan Michael, Elena Kuleshova, and David Ojala. 2016. 'A designer AAV variant permits efficient retrograde access to projection neurons', *Neuron*, 92: 372-82.

Thach, W Thomas, HP Goodkin, and JG Keating. 1992. 'The cerebellum and the adaptive coordination of movement', *Annual review of neuroscience*, 15: 403-42.

Thibeault, Corey M, and Narayan Srinivasa. 2013. 'Using a hybrid neuron in physiologically inspired models of the basal ganglia', *Frontiers in computational neuroscience*, 7: 88.

Thoma, Patrizia, Christian Bellebaum, Benno Koch, Michael Schwarz, and Irene Daum. 2008. 'The cerebellum is involved in reward-based reversal learning', *The Cerebellum*, 7: 433-43.

Tomita, Hiroshi, Eriko Sugano, Yugo Fukazawa, Hitomi Isago, Yuka Sugiyama, Teru Hiroi, Toru Ishizuka, Hajime Mushiake, Megumi Kato, and Masumi Hirabayashi. 2009. 'Visual

properties of transgenic rats harboring the channelrhodopsin-2 gene regulated by the thy-1.2 promoter', *PloS one*, 4: e7679.

Tsukahara, N, H Korn, and J Stone. 1968. 'Pontine relay from cerebral cortex to cerebellar cortex and nucleus interpositus', *Brain Research*, 10: 448-53.

Ueki, Yoshino, Tatsuya Mima, Mamdouh Ali Kotb, Hideyuki Sawada, Hidemoto Saiki, Akio Ikeda, Tahamina Begum, Faruque Reza, Takashi Nagamine, and Hidenao Fukuyama. 2006. 'Altered plasticity of the human motor cortex in Parkinson's disease', *Annals of neurology*, 59: 60-71.

Urbain, Nadia, Paul A Salin, Paul-Antoine Libourel, Jean-Christophe Comte, Luc J Gentet, and Carl CH Petersen. 2015. 'Whisking-related changes in neuronal firing and membrane potential dynamics in the somatosensory thalamus of awake mice', *Cell reports*, 13: 647-56.

Van Dijck, Gert, Marc M Van Hulle, Shane A Heiney, Pablo M Blazquez, Hui Meng, Dora E Angelaki, Alexander Arenz, Troy W Margrie, Abteen Mostofi, and Steve Edgley. 2013. 'Probabilistic identification of cerebellar cortical neurones across species', *PloS one*, 8: e57669.

Van Kan, Peter L, Alan R Gibson, and James C Houk. 1993. 'Movement-related inputs to intermediate cerebellum of the monkey', *Journal of neurophysiology*, 69: 74-94.

Wagner, Mark J, Tony Hyun Kim, Jonathan Kadmon, Nghia D Nguyen, Surya Ganguli, Mark J Schnitzer, and Liqun Luo. 2019. 'Shared cortex-cerebellum dynamics in the execution and learning of a motor task', *Cell*, 177: 669-82. e24.

Wang, Wenjing, Craig P Wildes, Tanyaporn Pattarabanjird, Mateo I Sanchez, Gordon F Glober, Gillian A Matthews, Kay M Tye, and Alice Y Ting. 2017. 'A light-and calcium-gated transcription factor for imaging and manipulating activated neurons', *Nature biotechnology*, 35: 864-71.

Wang, Yu, Xinxin Yin, Zhouzhou Zhang, Jiejue Li, Wenyu Zhao, and Zengcai V Guo. 2021. 'A cortico-basal ganglia-thalamo-cortical channel underlying short-term memory', *Neuron*, 109: 3486-99. e7.

Wu, H‐S, I Sugihara, and Y Shinoda. 1999. 'Projection patterns of single mossy fibers originating from the lateral reticular nucleus in the rat cerebellar cortex and nuclei', *Journal of Comparative Neurology*, 411: 97-118.

Wu, Xuanjing, Gideon A Sarpong, Jingyun Zhang, and Izumi Sugihara. 2023. 'Divergent topographic projection of cerebral cortical areas to overlapping cerebellar lobules through distinct regions of the pontine nuclei', *Heliyon*, 9.

Yagishita, Sho, Akiko Hayashi-Takagi, Graham CR Ellis-Davies, Hidetoshi Urakubo, Shin Ishii, and Haruo Kasai. 2014. 'A critical time window for dopamine actions on the

structural plasticity of dendritic spines', *Science*, 345: 1616-20.

Yamazaki, Tadashi, and William Lennon. 2019. 'Revisiting a theory of cerebellar cortex', *Neuroscience Research*, 148: 1-8.

Yasoshima, Yasunobu, Nobuyuki Kai, Shigetaka Yoshida, Sadao Shiosaka, Yoshimasa Koyama, Yukihiko Kayama, and Kazuto Kobayashi. 2005. 'Subthalamic neurons coordinate basal ganglia function through differential neural pathways', *Journal of Neuroscience*, 25: 7743-53.

Yoshida, Junichi, Maritza Oñate, Leila Khatami, Jorge Vera, Farzan Nadim, and Kamran Khodakhah. 2022. 'Cerebellar contributions to the basal ganglia influence motor coordination, reward processing, and movement vigor', *Journal of Neuroscience*, 42: 8406-15.

Yoshizawa, Tomohiko, Yuuto Miyamura, Yuta Ochi, Riichiro Hira, Makoto Funahashi, Yutaka Sakai, Yilong Cui, and Yoshikazu Isomura. 2023. 'Working memory-based and-free reward prediction in a dual dopamine system in the basal ganglia', *bioRxiv*: 2023.03.06.531239.

Zhu, Jia, Hana Hasanbegović, Liu D Liu, Zhenyu Gao, and Nuo Li. 2023. 'Activity map of a cortico-cerebellar loop underlying motor planning', *Nature neuroscience*, 26: 1916-28.

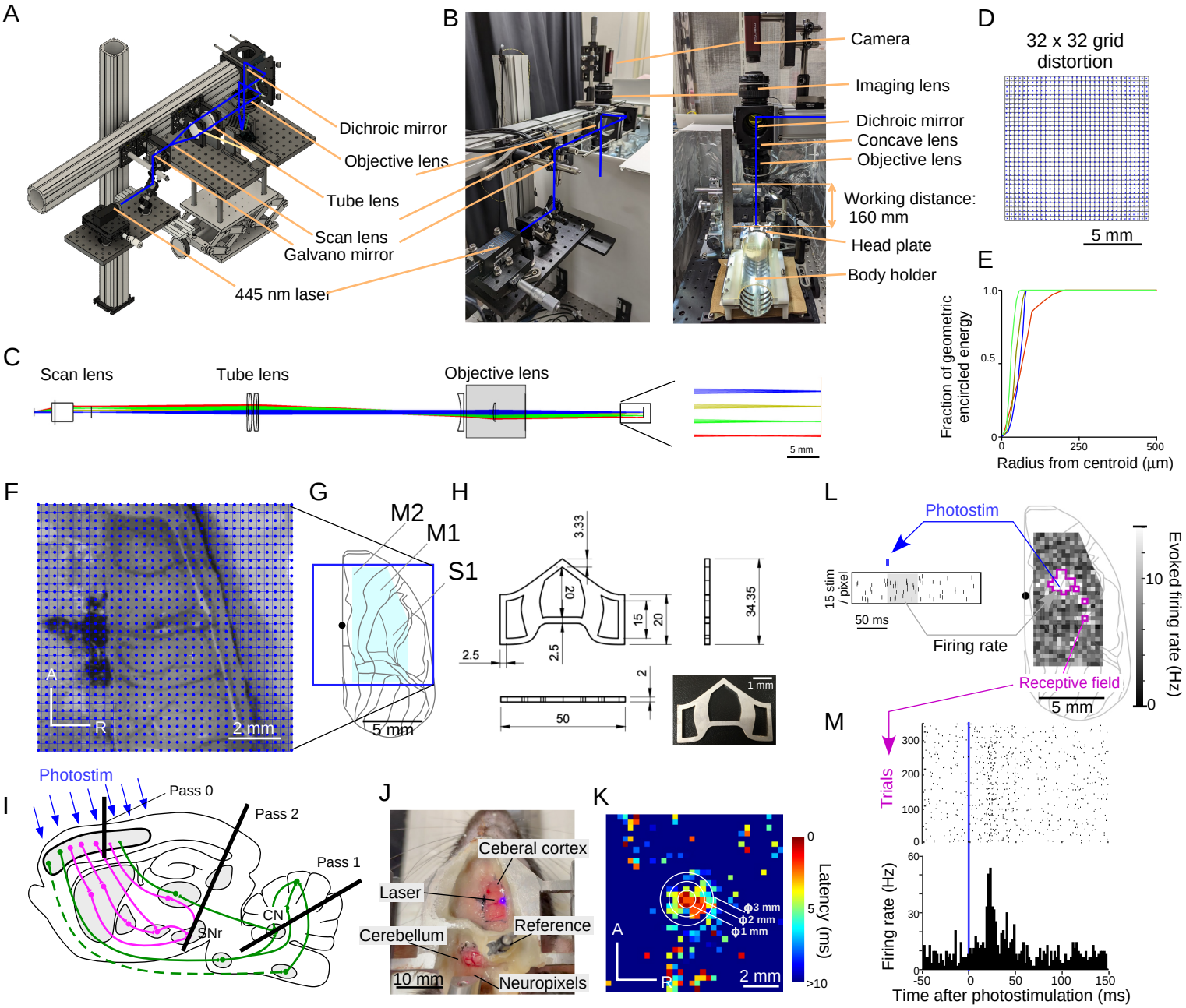
A
Dichroic mirror
Objective lens
Tube lens
Scan lens
Galvano mirror
445 nm laser
B
Camera
Imaging lens
Dichroic mirror
Concave lens
Objective lens
Working distance:
160 mm
Head plate
Body holder
D
32 x 32 grid
distortion
5 mm
E
Fraction of geometric
encircled energy
Radius from centroid (µm)
C
Scan lens
Tube lens
Objective lens
5 mm
F
A
R
2 mm
G
M2
M1
S1
5 mm
H
3.33
20
15
20
34.35
2.5
2.5
2
50
1 mm
L
Photostim
15 stim
/ pixel
50 ms
Firing rate
Receptive field
5 mm
Evoked firing rate (Hz)
M
Trials
Firing rate (Hz)
Time after photostimulation (ms)
I
Photostim
Pass 0
Pass 2
Pass 1
CN
SNr
J
Ceberal cortex
Laser
Reference
Cerebellum
10 mm
Neuropixels
K
ϕ3 mm
ϕ2 mm
ϕ1 mm
A
R
2 mm
Latency (ms)
>10

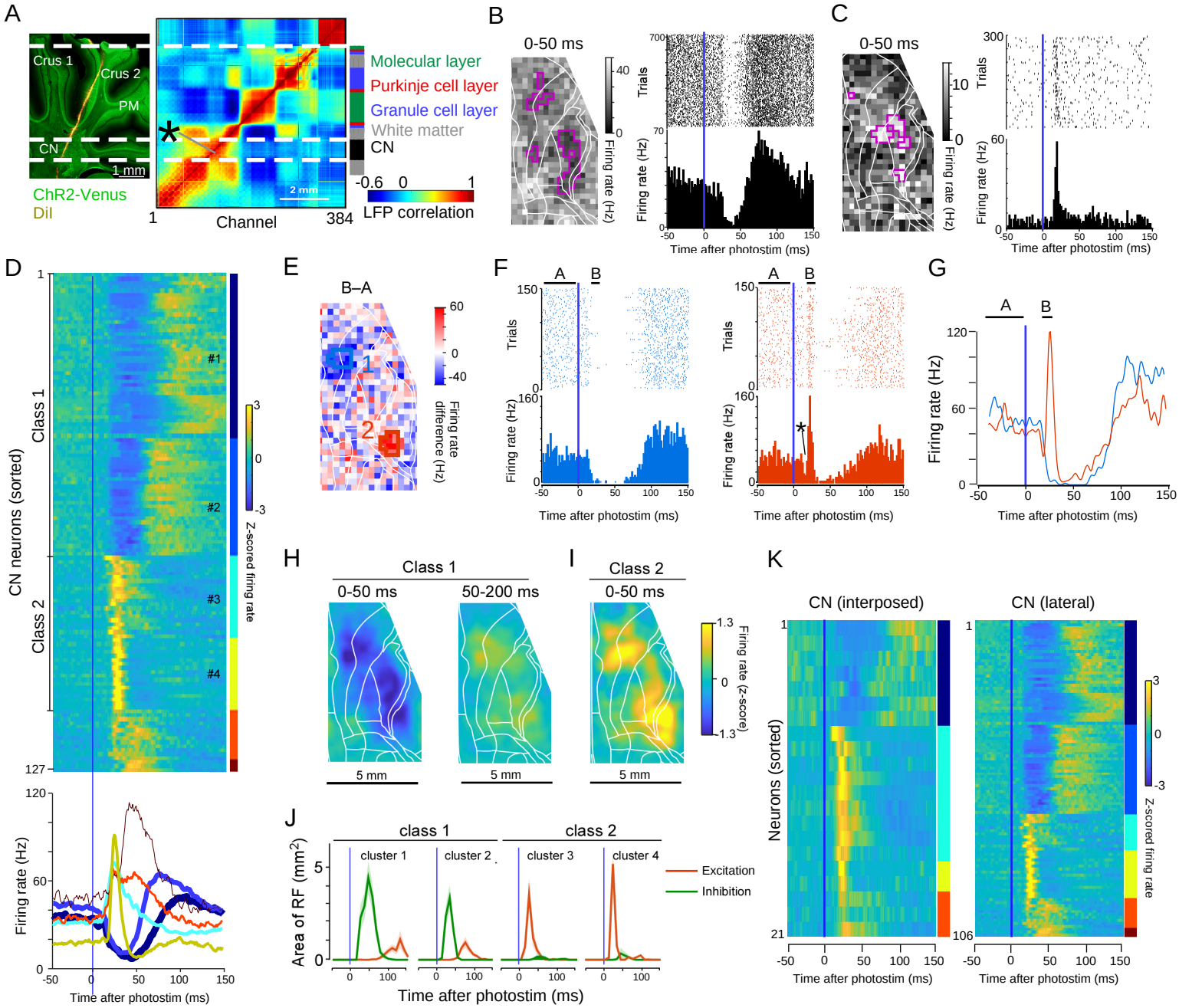
A
Crus 1
Crus 2
PM
CN
1 mm
ChR2-Venus
DiI
2 mm
1
Channel
384
Molecular layer
Purkinje cell layer
Granule cell layer
White matter
CN
-0.6 0 1
LFP correlation
B
0-50 ms
Trials
Firing rate (Hz)
Time after photostim (ms)
C
0-50 ms
Trials
Firing rate (Hz)
Time after photostim (ms)
D
CN neurons (sorted)
Class 1
Class 2
#1
#2
#3
#4
Z-scored firing rate
Firing rate (Hz)
Time after photostim (ms)
E
B–A
Firing rate difference (Hz)
F
A
B
Trials
Firing rate (Hz)
Time after photostim (ms)
G
A
B
Firing rate (Hz)
Time after photostim (ms)
H
Class 1
0-50 ms
50-200 ms
5 mm
I
Class 2
0-50 ms
Firing rate (z-score)
J
class 1
class 2
cluster 1
cluster 2
cluster 3
cluster 4
Area of RF (mm²)
Excitation
Inhibition
Time after photostim (ms)
K
CN (interposed)
CN (lateral)
Neurons (sorted)
Z-scored firing rate
Time after photostim (ms)

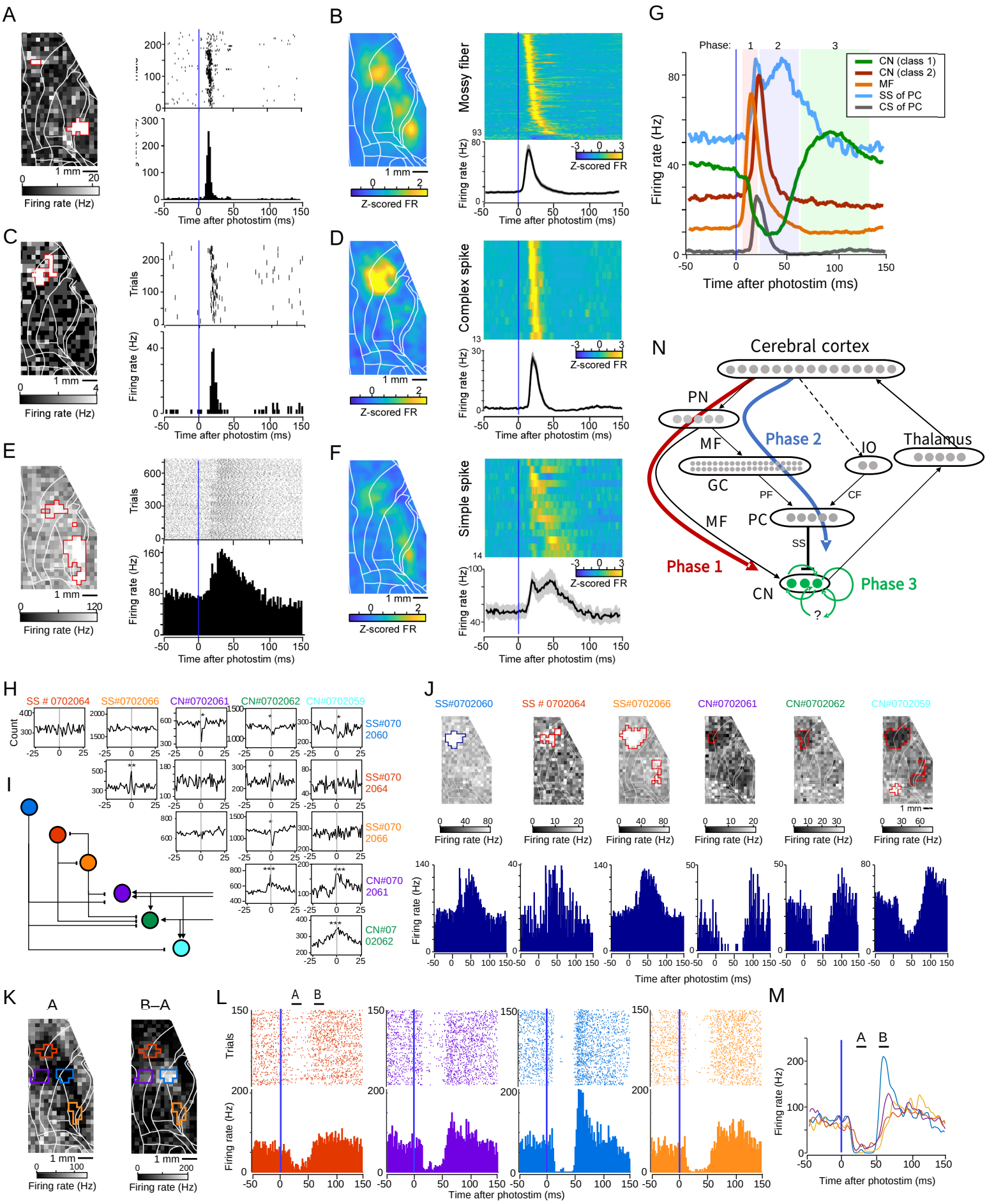
A
B
C
D
E
F
G
H
I
J
K
L
M
N
Mossy fiber
Complex spike
Simple spike
Trials
Firing rate (Hz)
Time after photostim (ms)
Z-scored FR
1 mm
Phase:
CN (class 1)
CN (class 2)
MF
SS of PC
CS of PC
Cerebral cortex
PN
MF
GC
PC
IO
Thalamus
CN
PF
CF
SS
Phase 1
Phase 2
Phase 3
SS # 0702064
SS#0702066
CN#0702061
CN#0702062
CN#0702059
SS#0702060
Count
SS#070 2060
SS#070 2064
SS#070 2066
CN#070 2061
CN#07 02062
A
B–A

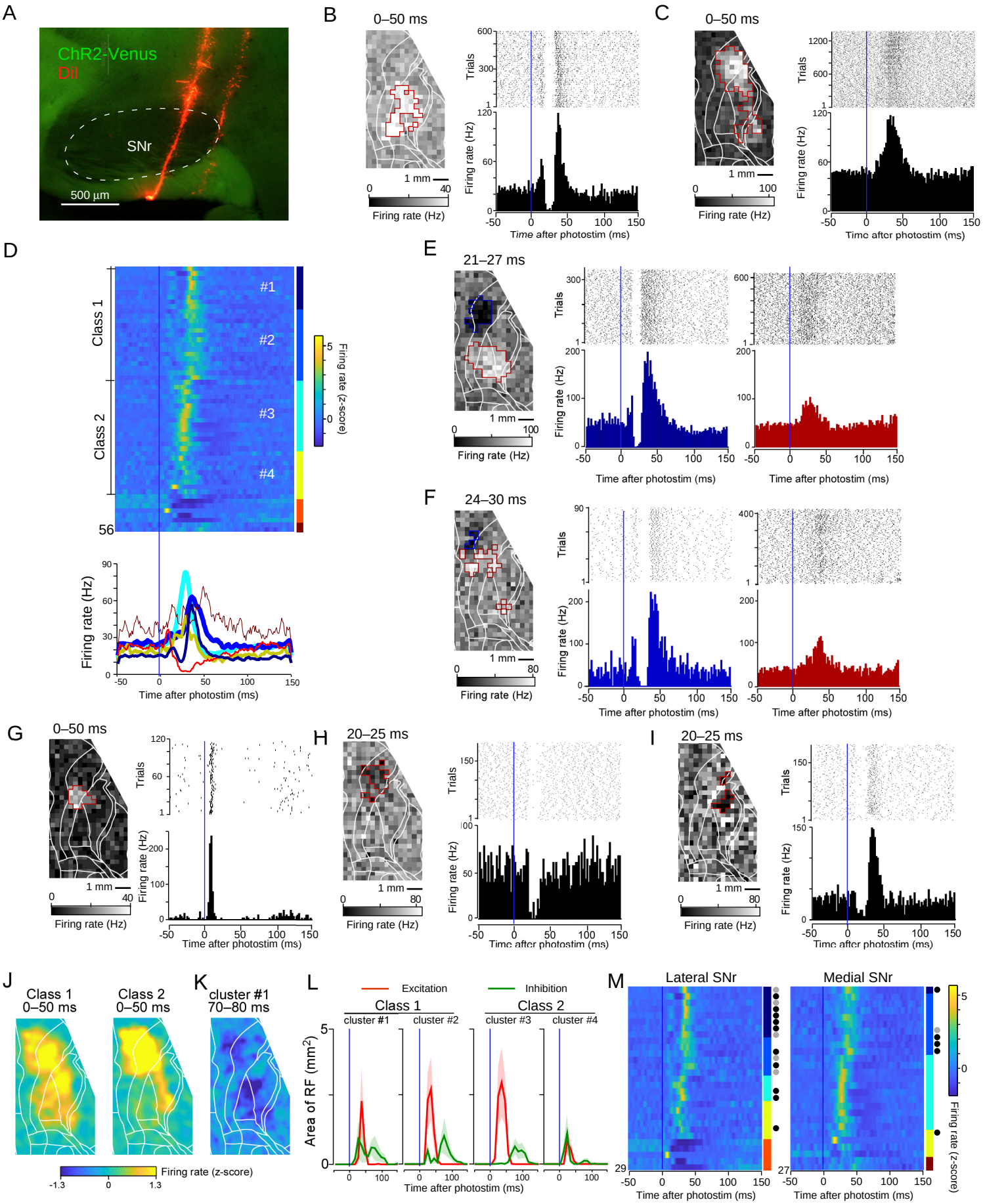
A
ChR2-Venus
DiI
SNr
500 µm
B
0–50 ms
1 mm
Firing rate (Hz)
Trials
Time after photostim (ms)
C
0–50 ms
D
Class 1
Class 2
#1
#2
#3
#4
Firing rate (z-score)
Time after photostim (ms)
E
21–27 ms
F
24–30 ms
G
0–50 ms
H
20–25 ms
I
20–25 ms
J
Class 1
0–50 ms
Class 2
0–50 ms
K
cluster #1
70–80 ms
Firing rate (z-score)
L
Excitation
Inhibition
Class 1
Class 2
cluster #1
cluster #2
cluster #3
cluster #4
Area of RF (mm²)
Time after photostim (ms)
M
Lateral SNr
Medial SNr
Firing rate (z-score)

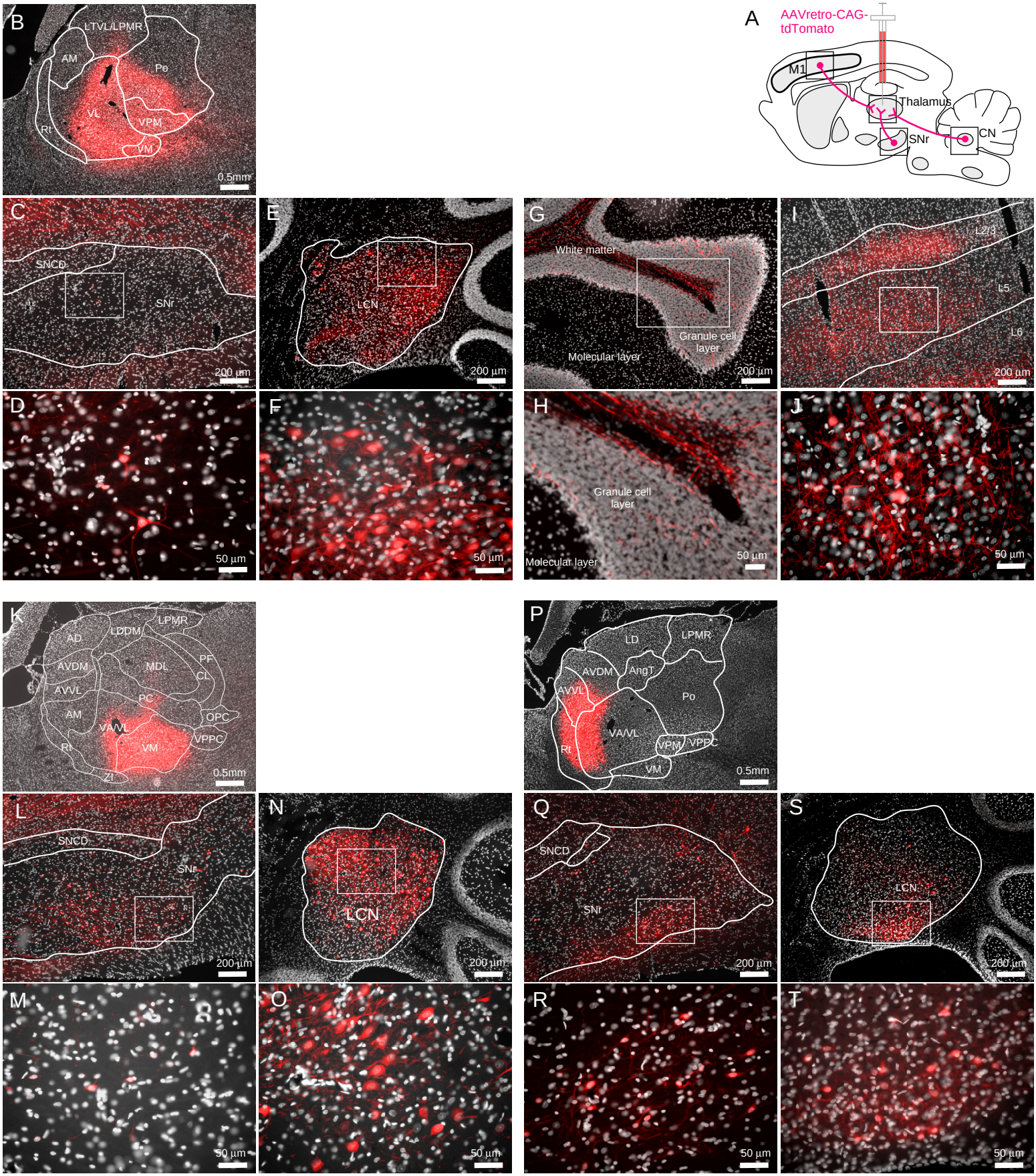
A
AAVretro-CAG-tdTomato
M1
Thalamus
SNr
CN
B
LTVL/LPMR
AM
Po
VL
VPM
Rt
VM
0.5mm
C
SNCD
SNr
200 µm
D
50 µm
E
LCN
200 µm
F
50 µm
G
White matter
Granule cell layer
Molecular layer
200 µm
H
Granule cell layer
Molecular layer
50 µm
I
L2/3
L5
L6
200 µm
J
50 µm
K
LPMR
AD
LDDM
PF
AVDM
MDL
CL
AVVL
PC
AM
OPC
VA/VL
VPPC
Rt
VM
ZI
0.5mm
L
SNCD
SNr
200 µm
M
50 µm
N
LCN
200 µm
O
50 µm
P
LD
LPMR
AVDM
AngT
AVVL
Po
VA/VL
Rt
VPM
VPPC
VM
0.5mm
Q
SNCD
SNr
200 µm
R
50 µm
S
LCN
200 µm
T
50 µm

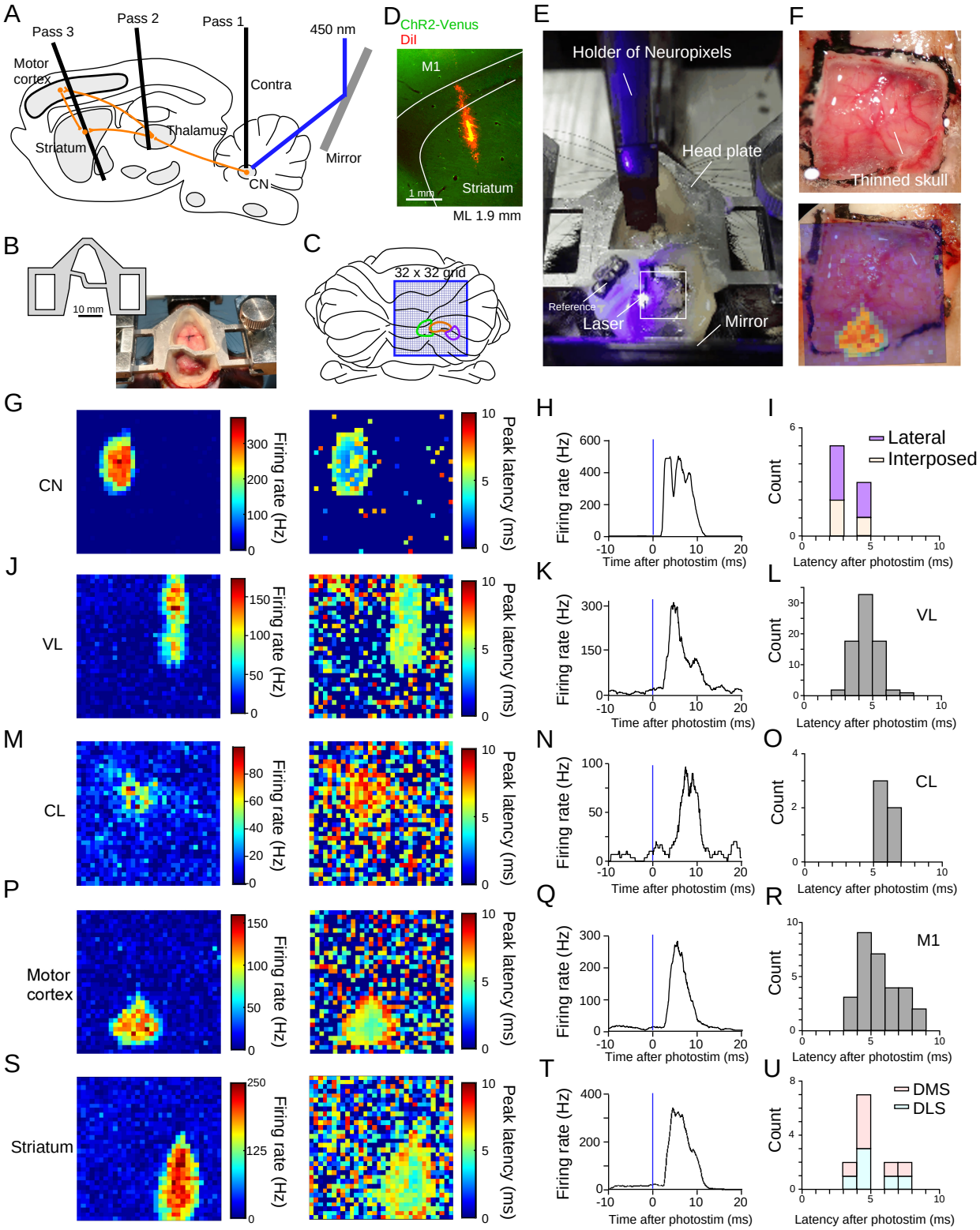
A
Pass 3
Pass 2
Pass 1
450 nm
Motor cortex
Contra
Thalamus
Striatum
CN
Mirror
D
ChR2-Venus
DiI
M1
1 mm
Striatum
ML 1.9 mm
E
Holder of Neuropixels
Head plate
Reference
Laser
Mirror
F
Thinned skull
B
10 mm
C
32 x 32 grid
G
CN
Firing rate (Hz)
Peak latency (ms)
J
VL
M
CL
P
Motor cortex
S
Striatum
H
Firing rate (Hz)
Time after photostim (ms)
I
Lateral
Interposed
Count
Latency after photostim (ms)
K
L
VL
N
O
CL
Q
R
M1
T
U
DMS
DLS

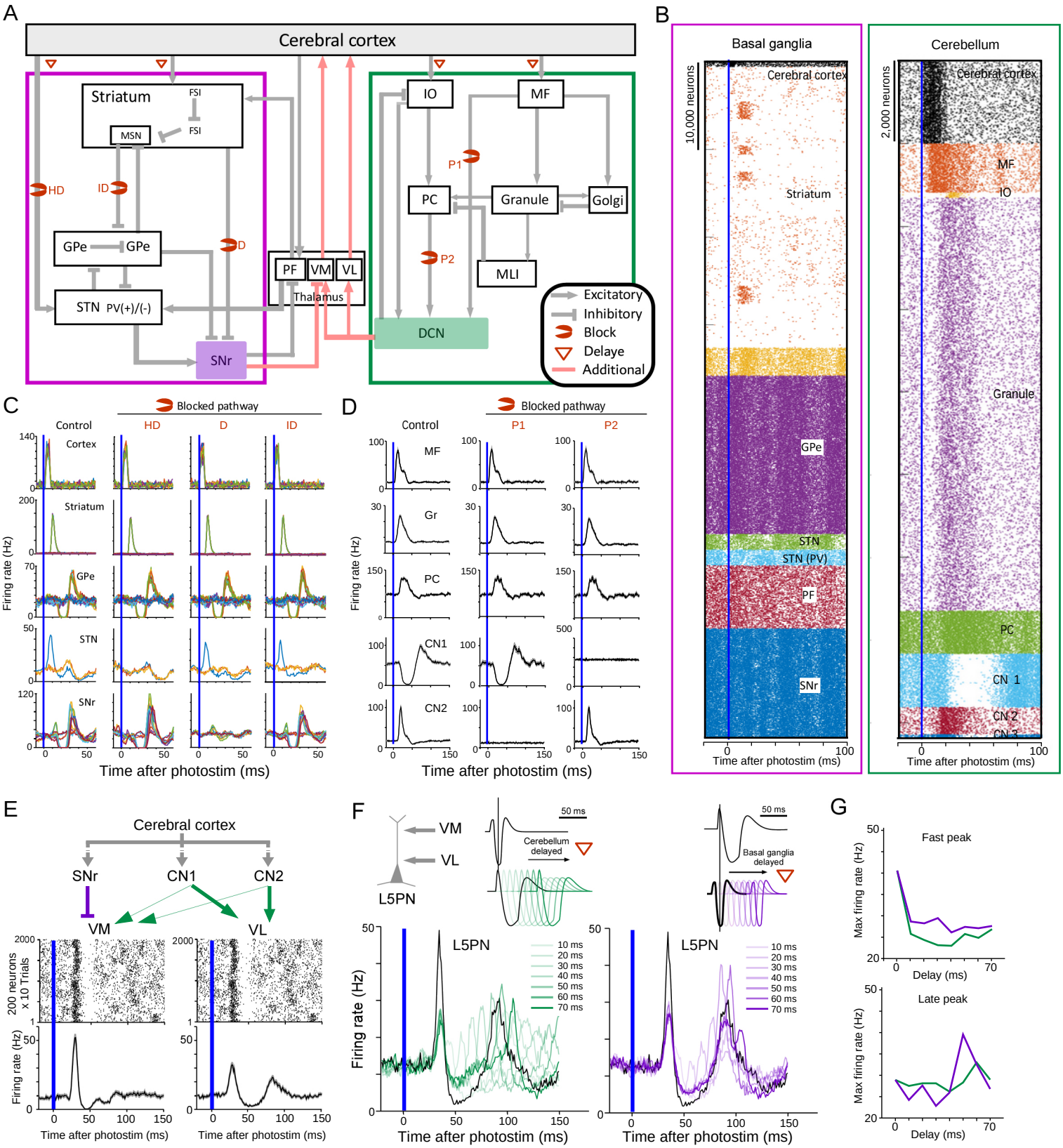
A
Cerebral cortex
Striatum
FSI
MSN
FSI
HD
ID
GPe
GPe
D
STN PV(+)/(-)
SNr
PF
VM
VL
Thalamus
IO
MF
P1
PC
Granule
Golgi
P2
MLI
DCN
Excitatory
Inhibitory
Block
Delaye
Additional
B
Basal ganglia
10,000 neurons
Cerebral cortex
Striatum
GPe
STN
STN (PV)
PF
SNr
Time after photostim (ms)
Cerebellum
2,000 neurons
Cerebral cortex
MF
IO
Granule
PC
CN 1
CN 2
CN 3
Time after photostim (ms)
C
Blocked pathway
Control
HD
D
ID
Cortex
Striatum
GPe
STN
SNr
Firing rate (Hz)
Time after photostim (ms)
D
Blocked pathway
Control
P1
P2
MF
Gr
PC
CN1
CN2
Firing rate (Hz)
Time after photostim (ms)
E
Cerebral cortex
SNr
CN1
CN2
VM
VL
200 neurons x 10 Trials
Firing rate (Hz)
Time after photostim (ms)
Time after photostim (ms)
F
VM
VL
L5PN
50 ms
Cerebellum delayed
50 ms
Basal ganglia delayed
L5PN
10 ms
20 ms
30 ms
40 ms
50 ms
60 ms
70 ms
Firing rate (Hz)
Time after photostim (ms)
Time after photostim (ms)
G
Fast peak
Max firing rate (Hz)
Delay (ms)
Late peak
Max firing rate (Hz)
Delay (ms)

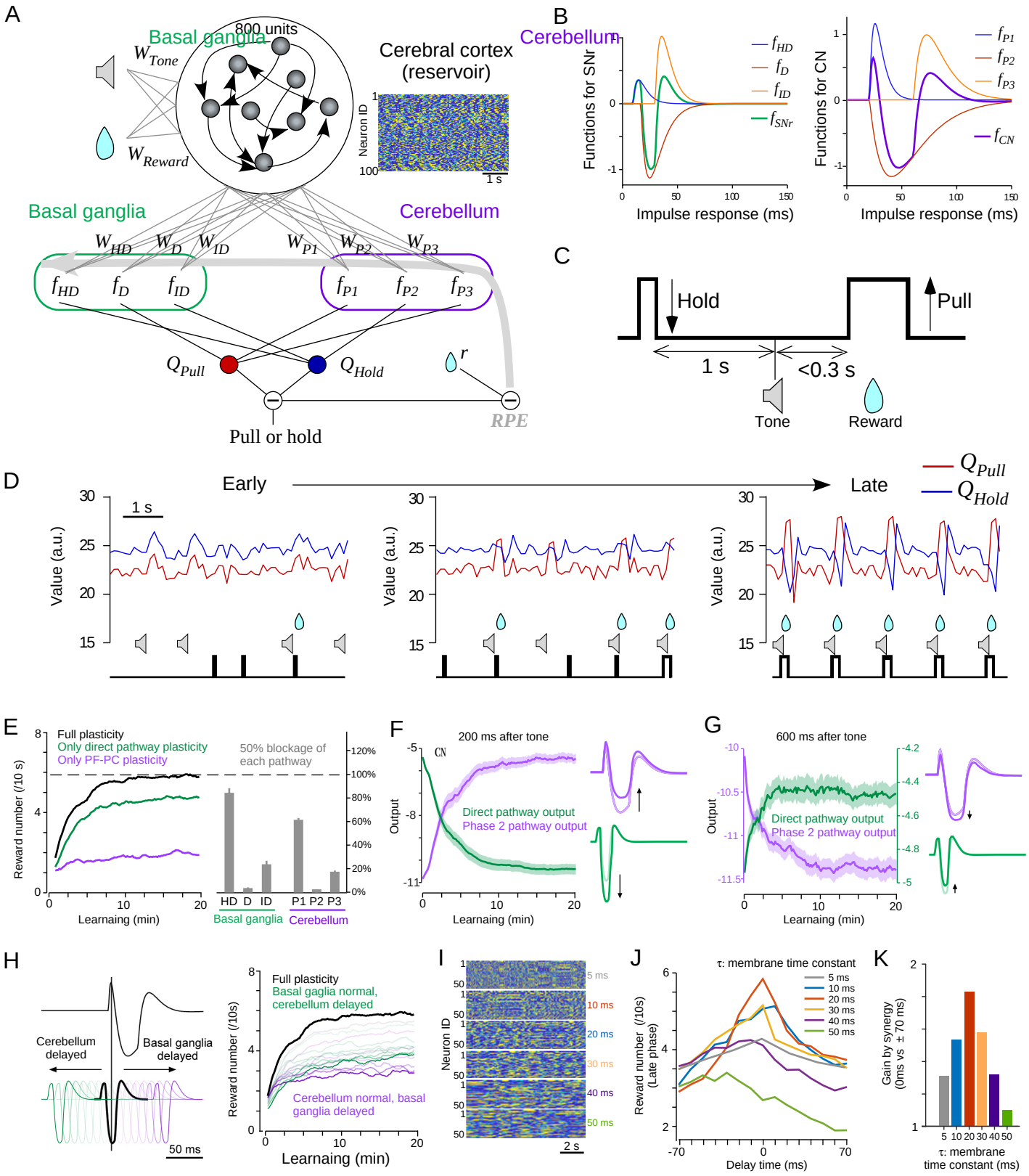
A
Basal ganglia
800 units
W_{Tone}
W_{Reward}
Cerebral cortex
(reservoir)
Neuron ID
1 s
Basal ganglia
Cerebellum
W_{HD} W_D W_{ID} W_{P1} W_{P2} W_{P3}
f_{HD} f_D f_{ID} f_{P1} f_{P2} f_{P3}
Q_{Pull} Q_{Hold} r
RPE
Pull or hold
B
Cerebellum
Functions for SNr
f_{HD} f_D f_{ID} f_{SNr}
Impulse response (ms)
Functions for CN
f_{P1} f_{P2} f_{P3} f_{CN}
Impulse response (ms)
C
Hold
Pull
1 s
<0.3 s
Tone
Reward
D
Early
Late
Q_{Pull}
Q_{Hold}
Value (a.u.)
1 s
E
Full plasticity
Only direct pathway plasticity
Only PF-PC plasticity
Reward number (/10 s)
Learnaing (min)
50% blockage of each pathway
HD D ID
P1 P2 P3
Basal ganglia
Cerebellum
F
200 ms after tone
CN
Output
Direct pathway output
Phase 2 pathway output
Learnaing (min)
G
600 ms after tone
Output
Direct pathway output
Phase 2 pathway output
Learnaing (min)
H
Cerebellum delayed
Basal ganglia delayed
50 ms
Full plasticity
Basal gaglia normal, cerebellum delayed
Cerebellum normal, basal ganglia delayed
Reward number (/10s)
Learnaing (min)
I
Neuron ID
5 ms
10 ms
20 ms
30 ms
40 ms
50 ms
2 s
J
τ: membrane time constant
5 ms
10 ms
20 ms
30 ms
40 ms
50 ms
Reward number (/10s) (Late phase)
Delay time (ms)
K
Gain by synergy (0ms vs ± 70 ms)
τ: membrane time constant (ms)

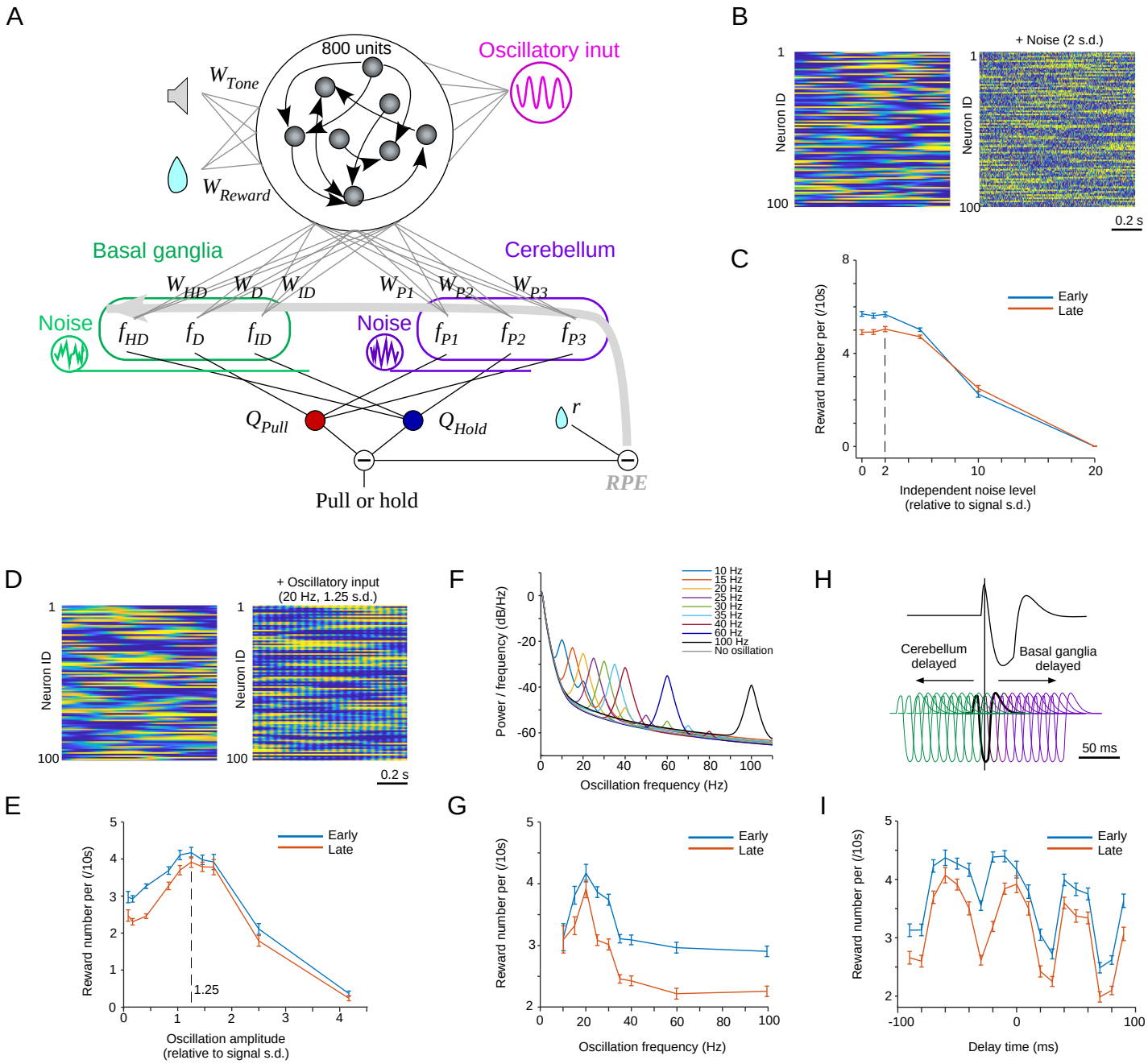
A
800 units
Oscillatory inut
W_{Tone}
W_{Reward}
Basal ganglia
Cerebellum
W_{HD} W_D W_{ID}
W_{P1} W_{P2} W_{P3}
Noise
f_{HD} f_D f_{ID}
Noise
f_{P1} f_{P2} f_{P3}
Q_{Pull}
Q_{Hold}
r
RPE
Pull or hold
B
+ Noise (2 s.d.)
Neuron ID
1
100
0.2 s
C
Reward number per (/10s)
Early
Late
Independent noise level
(relative to signal s.d.)
D
+ Oscillatory input
(20 Hz, 1.25 s.d.)
Neuron ID
0.2 s
E
Reward number per (/10s)
Early
Late
1.25
Oscillation amplitude
(relative to signal s.d.)
F
Power / frequency (dB/Hz)
10 Hz
15 Hz
20 Hz
25 Hz
30 Hz
35 Hz
40 Hz
60 Hz
100 Hz
No osillation
Oscillation frequency (Hz)
G
Reward number per (/10s)
Early
Late
Oscillation frequency (Hz)
H
Cerebellum
delayed
Basal ganglia
delayed
50 ms
I
Reward number per (/10s)
Early
Late
Delay time (ms)